NACA RM L52D04

NACA

RESEARCH MEMORANDUM

LOW-SPEED WIND-TUNNEL INVESTIGATION OF THE EFFECTS OF PROPELLER OPERATION AT HIGH THRUST ON THE LONGITUDINAL STABILITY AND TRIM OF A TWIN-ENGINE AIRPLANE CONFIGURATION

By William C. Sleeman, Jr. and Edward L. Linsley

Langley Aeronautical Laboratory
Langley Field, Va.

NATIONAL ADVISORY COMMITTEE FOR AERONAUTICS

WASHINGTON
July 14, 1952

NACA RM L52D04

NATIONAL ADVISORY COMMITTEE FOR AERONAUTICS

RESEARCH MEMORANDUM

LOW-SPEED WIND-TUNNEL INVESTIGATION OF THE EFFECTS OF PROPELLER OPERATION AT HIGH THRUST ON THE LONGITUDINAL STABILITY AND TRIM OF A TWIN-ENGINE AIRPLANE CONFIGURATION

By William C. Sleeman, Jr. and Edward L. Linsley

SUMMARY

An investigation has been made to determine the effects of dual-rotation propeller operation at high thrust on the static longitudinal stability characteristics of a semispan powered model representing a twin-engine airplane configuration with flaps retracted. The flow field behind the model was studied extensively by several techniques which provided information relating to the tail contribution to over-all stability characteristics.

Stability and trim changes associated with an extreme constant power condition were found to be greatly dependent upon both tail height and vertical location of the center of gravity. Large adverse effects of power were obtained for a configuration having the center of gravity located on the thrust line and the tail in a high position. It was found that adverse power effects could be essentially eliminated either by moving the tail down into the slipstream or by utilization of the direct-propeller-thrust moment associated with a vertical displacement of the center of gravity to provide stability.

The lift effectiveness of the tail located in the propeller slipstream was found to increase with the slipstream velocity ratio to the first power rather than to increase directly with the dynamic pressure ratio.

The basic-force results indicated that the lift-curve slope of the complete model increased with thrust up to the highest test value of thrust coefficient. The increment of wing-lift slope due to power, however, reached a maximum near a thrust coefficient of unity and diminished with further increases of thrust. At the highest thrust coefficient investigated, about 90 percent of the lift-slope increase of the complete

model was associated with the direct propeller forces. Power-on downwash angles showed fairly consistent increases with thrust coefficient when the thrust line was located at one-third of the wing semispan; whereas results obtained with the propeller at the midsemispan of the wing showed only small changes in downwash angle due to power and did not vary appreciably with thrust.

INTRODUCTION

Many experimental investigations have been made to determine slipstream effects on specific multi-engine airplane configurations. These results, however, have generally been limited in the range of geometric variables studied and in the amount of power simulated. The need for general research information for extreme power conditions became apparent with the development of turbine-propeller engines and the present investigation was undertaken as a step toward filling this need. Results of this investigation afford information relating to the effects of propeller operation at very high thrust coefficients on the longitudinal characteristics of a twin-engine airplane configuration with flaps retracted.

Aerodynamic characteristics of the semispan model, which had a dual-rotation propeller, were obtained for values of constant thrust from $T_c = 0$ up to $T_c = 2.5$. A general study was also made to determine slipstream effects on the flow characteristics in the region of the horizontal tail. Downwash angles were obtained from several free-floating tails mounted behind the model, and dynamic pressure ratios were obtained from survey rakes attached to the model. These results afforded flow information for a wide range of tail heights. A fixed horizontal tail was attached to the model in order to check the flow results obtained from the floating tails and rake surveys and to obtain an over-all evaluation of power effects on an assumed complete airplane configuration.

Surveys were also made by using a tuft grid behind the model to obtain an over-all picture of the flow angularity and the extent of the slipstream near the plane of the horizontal tail.

COEFFICIENTS AND SYMBOLS

The basic results of this investigation are presented as standard NACA coefficients of forces and moments referred to the wind axes. Pitching-moment coefficients are referred to an axis through the wing $\bar{c}/4$ on the wing chord plane.

[redacted]

C_L	lift coefficient $\left(\frac{\text{Twice semispan lift}}{q_o S}\right)$
C_{L_W}	wing-lift coefficient (lift component of propeller thrust not included)
C_X	longitudinal-force coefficient $\left(\frac{\text{Twice semispan longitudinal force}}{q_o S}\right)$
C_D	drag coefficient $\left(-C_X\right)$
C_m	pitching-moment coefficient $\left(\frac{\text{Twice semispan pitching-moment}}{q_o S \bar{c}}\right)$
C_B	bending-moment coefficient due to lift, about root chord line (at plane of symmetry) $\left(\frac{\text{Root bending moment}}{q_o \frac{S}{2} \frac{b}{2}}\right)$
T_c	effective-thrust coefficient $\left(\frac{T_e}{\rho V^2 D^2}\right)$
T_e	effective thrust, pounds
q_o	free-stream dynamic pressure, pounds per square foot $\left(\frac{1}{2}\rho V^2\right)$
ρ	air density, slugs per cubic foot
V	free-stream velocity, feet per second
S	twice wing area of semispan model, square feet
b	twice wing span of semispan model, feet; also propeller blade section chord, feet
$\bar{c}$	mean aerodynamic chord of wing, feet
D	propeller diameter, feet
R	propeller radius, feet

[redacted]

r	radius to any propeller blade element, feet
h	propeller blade section thickness, feet
n	propeller rotational speed, revolutions per second
V/nD	propeller advance-diameter ratio
h_t	tail height above wing-chord plane, percent wing semispan
y_{cp}	lateral center of pressure, percent wing semispan $(100C_B/C_L)$
α	angle of attack, degrees
α_g	geometric angle of attack, degrees
ϵ	downwash angle, degrees
i_t	incidence of horizontal tail relative to wing chord line, degrees (positive when trailing edge is down)
β	propeller blade angle, degrees
q/q_o	ratio of local dynamic pressure to free-stream dynamic pressure
R_t	tail-lift effectiveness ratio obtained from ratio of $\left(\frac{\partial C_m}{\partial i_t}\right)$ to the maximum power-off value of $\left(\frac{\partial C_m}{\partial i_t}\right)$ as determined from force tests. (Also obtained from integrated dynamic pressure ratios from flow surveys.)
l_t	longitudinal distance between quarter-chord lines of wing and horizontal tail, feet
ΔC_D	drag coefficient due to lift $\left(C_D - (C_D)_{C_L=0}\right)$
$(C_D)_{C_L=0}$	drag coefficient at zero lift
$(C_m)_{\alpha=0}$	pitching-moment coefficient at an angle of attack of 0°

$\left(\frac{\partial C_m}{\partial C_L}\right)_{T_c}$, $\left(\frac{\partial C_L}{\partial \alpha}\right)_{T_c}$ slopes measured at a constant thrust coefficient

Abbreviation:

Prop. off propeller removed

MODEL AND APPARATUS

The model used in this investigation had an unswept wing of aspect ratio 9, taper ratio 0.5, and had NACA 64_1A012 airfoil sections parallel to the free stream. Drawings of the model showing the configuration tested and pertinent dimensions are presented in figure 1. A photograph of the model installed in the Langley 300 MPH 7- by 10-foot tunnel is given as figure 2. The semispan model was mounted from the tunnel ceiling with a gap between the fuselage and ceiling of approximately 3/16 inch. For all tests the center line of the fuselage was on the wing-chord plane.

Geometric characteristics of the six-blade dual-rotation propeller used in this investigation are given in figure 3. The propeller was 28.33 inches in diameter and was driven by means of a dual-rotation gear box mounted on the front of a 56-horsepower electric motor. The motor was located in a nacelle on the lower surface of the wing. The rotational speed of the propeller was determined by observation of a cathode-ray oscillograph which indicated the output frequency of a small alternator connected to the shaft of the motor. For all power-on tests the propeller blades were set at an angle of 11.3° at the 0.75 radius station.

Two spanwise locations of the thrust line were tested; the inboard position was at one-third of the wing semispan and the outboard position was at the midsemispan.

The basic data of this investigation were obtained without a horizontal tail mounted on the model. Four free-floating tails were located behind, and independently of, the model to obtain effective downwash angles concurrently with the basic tail-off force data. Additional tests were made with one of these tails attached rigidly to the fuselage. For these tests the fuselage was extended 19 inches to support the fixed tail as shown by the broken lines in figure 1. The tail was located on the wing-chord plane and the distance between the quarter-chord lines of the wing and tail was 92 percent of the wing semispan $\left(\frac{l_t}{\bar{c}} = 4.0\right)$.

[redacted]

Both the fixed tail and the floating tails were constructed of $\frac{1}{2}$-inch-thick plywood and were of aspect ratio 5.55 and taper ratio 0.50. The leading edge and tip section of the tails were rounded with a $\frac{1}{4}$-inch radius.

The floating tails used in the flow surveys were mounted through the tunnel ceiling and were supported by bearings which allowed the tails to pivot freely. Effective downwash angles were measured by use of calibrated slide-wire potentiometers connected to the pivot shaft of each tail. Dynamic-pressure measurements were obtained from 0.04-inch outside-diameter steel total-pressure tubes protruding 1 inch from the leading edge of the tails. These tubes were connected to a manometer by flexible tubing through a $\frac{3}{4}$-inch-diameter tubular pivot shaft. Tests with and without the flexible tubing connected externally indicated that the floating angles were not affected by this tubing.

Additional dynamic-pressure surveys were made by using several total-pressure rakes attached to the extended fuselage approximately in the plane of the total-pressure tubes on the floating tails. These tests were made to obtain more detailed slipstream definition than could be obtained from the widely spaced floating tails.

Flow studies were also made by use of a tuft grid similar to the one used in the tests of reference 1. The tuft grid was placed slightly downstream of the horizontal tail location (1.1 wing semispans behind the wing quarter-chord line) and extended over most of the tunnel cross section. Woolen tufts about 1/8 inch in diameter and 6 inches long were attached to each intersection of the 0.03-inch-diameter wires which were spaced 2 inches apart both horizontally and vertically. Even spacing of the grid was maintained by interlacing the wires and soldering each intersection. A spring was attached to one end of each wire in order to retain a preload on the wires after the grid was subjected to deflection by air load. The tufts were allowed to swing freely by means of a thread loop fastened to the tuft and tied around the wire intersections, and the downstream end of each tuft was tied with thread to prevent the strands of wool from unraveling.

Photographs of the tuft grid were obtained by a camera mounted 75 feet downstream of the grid and approximately on the tunnel center line.

TESTS AND RESULTS

Test conditions.- All tests were made in the Langley 300 MPH 7- by 10-foot tunnel at a dynamic pressure of 4.0 pounds per square foot, corresponding to an airspeed of about 40 miles per hour. The test Reynolds number was approximately 0.55×10^6 based on a wing mean aerodynamic chord of 1.38 feet. The low tunnel speed used in the tests was necessary in order to obtain the maximum thrust coefficients desired. Some penalty in balance accuracy in measuring forces and moments at this tunnel speed was anticipated, and the tail-off tests at lower thrust coefficients were repeated at a dynamic pressure of 8.0 pounds per square foot. The force and moment data and the downwash results at a given thrust coefficient were in very good agreement for the tests run at $q_o = 8.0$ and $q_o = 4.0$. Results for only the latter value, therefore, are presented because of the large range of thrust coefficients obtained at this tunnel speed.

Test procedure.- The basic data were obtained with the angle of attack varied from -2° to 12° and with the thrust coefficient held constant. Power-off tests were made with the propeller removed and a wooden spinner mounted on the propeller shaft. Simultaneous readings of the forces and moments on the model, the tail floating angles, and total pressures at the tail were obtained at each angle of attack.

The propeller was calibrated by measuring the resultant longitudinal force of the model at an angle of attack of 0° for a range of propeller speeds with the tail removed. Effective thrust coefficients were computed from the following relationships:

$$T_e = X_R - X_o$$

$$T_c = \frac{T_e}{\rho V^2 D^2}$$

where X_o is the longitudinal force of the model with the propeller removed and X_R is the resultant longitudinal force obtained with the propeller operating. Results of the propeller calibration are presented in figure 4 which shows the variation of effective thrust coefficient with the propeller advance-diameter ratio. Some of the power-on tests simulated a constant power flight condition which was based on an operating chart obtained without the horizontal tail. For these tests the propeller speed and angle of attack of the model were adjusted to

correspond to the assumed relationship of T_c and C_L given in figure 5. The horsepower represented in these tests is given in figure 6 as a function of airplane wing loading and size. A propeller efficiency of 70 percent was assumed and the altitude was taken as sea level in computing the relationships of figures 5 and 6.

Corrections.- Jet-boundary corrections to the angles of attack and longitudinal-force coefficients were obtained from reference 2. The following corrections were added to the data:

$$\Delta\alpha = 0.858C_{L_W}(\text{degrees})$$

$$\Delta C_X = -0.015C_{L_W}{}^2$$

where

$$C_{L_W} = C_L - (\Delta C_L)_{\text{propeller thrust}}$$

Inasmuch as jet-boundary-induced upwash for tail positions considerably above and below the wing-chord plane were not available for application to the present tests, these corrections were evaluated and are given in appendix A.

Downwash angles obtained from the floating tails were corrected for tunnel flow-angularity by the use of the observed floating angles obtained with the model removed from the tunnel. A comparison of the results of tests of the model over the angle-of-attack range with only one floating tail with results obtained with four tails indicated that there was no interference between the four floating tails used in the tests.

Results.- The figures presenting the results are as follows:

DISCUSSION

Basic Data

The discussion of basic tail-off force and moment results is based on the summary of results presented in figure 9 which applies to both locations of the thrust line. Although small differences may be present for the two thrust locations, the summary curves presented represent closely the over-all characteristics of both configurations. Of course differences in lateral center of pressure would be expected as indicated in figure 9.

Lift.- The variation of lift-curve slope with thrust coefficient shows that, at the highest thrust coefficient attained, the lift slope of the complete model is almost twice that obtained with the propeller removed (fig. 9). Estimation of the lift component due to inclination of the thrust axis, however, indicated that, at the highest T_c, about 90 percent of the lift-slope increase was associated with the direct propeller forces. Experimental results for the wing contribution to the power-on lift slopes were obtained by subtracting the lift component of propeller thrust from the complete model results. The wing-lift increment due to power is seen to increase up to about $T_c = 1.0$ and decrease with increasing thrust for thrust coefficients above $T_c = 1.4$.

Estimated wing-lift slopes derived from reference 3 are in good agreement with the experimental results up to about $T_c = 1.0$. At higher values of T_c the computed slopes are somewhat higher than those obtained from the test data. Since the method of reference 3 is based, in part,

on empirical values obtained from tests at fairly low thrust coefficients, the departure from experiment at high slipstream velocities is not surprising.

The complex flow phenomena associated with the propeller slipstream and the wing impose formidable difficulties in evaluating slipstream effects on wing lift for a wide range of thrust coefficients. It thus appears that more test results at high thrust coefficients for a number of configurations would afford a rational basis for extending the applicability of the empirical method of reference 3.

Pitching moment.- The variation of pitching-moment slope $\partial C_m/\partial C_L$ with thrust coefficient (fig. 9) shows a forward movement of the aerodynamic center of approximately 8 percent $\bar{c}$ from propeller-off to maximum T_c. Tests made with the propeller windmilling indicated that approximately 3 percent $\bar{c}$ of this forward shift was associated with the contribution of the propeller rotating near zero thrust. The estimated curve was obtained by addition of the pitching-moment slope increment due to the propeller normal force (reference 4) to the basic propeller-off pitching-moment slope. The differences shown between experimental and estimated propeller effects on $\partial C_m/\partial C_L$ suggest that factors other than the direct propeller contribution may have been significant. It is believed that the estimated curve represents the direct propeller contribution fairly well in view of the good agreement of the estimated value at $T_c = 0$ with the experimental slope obtained with the propeller windmilling $\left(\frac{\partial C_m}{\partial C_L} = 0.11\right)$.

The vertical location of the center of gravity was above the thrust line and consequently large changes in pitching moment at an angle of attack of 0° were evident as the thrust coefficient increased. Estimated values of $(C_m)_{\alpha=0}$ compare favorably with test results throughout the range of thrust coefficients tested. A slight departure exists above $T_c = 1.2$ which is probably related to increased drag for that part of the wing immersed in the slipstream.

Lateral center of pressure.- The lateral center of pressure y_{cp} for the clean wing without the nacelle was located at 44 percent of the wing semispan. When the thrust line was at $0.33b/2$, y_{cp} moved inboard with increasing thrust and similarly shifted outboard when the thrust line was at $0.50b/2$. The estimated curves were obtained by assuming that the incremental lift due to power for the complete model was concentrated at the thrust line and that the power-off lift acted at the lateral center of pressure for $T_c = 0$. The estimated results compare favorably with the test data throughout the thrust-coefficient range.

[redacted]

Drag due to lift.- Slipstream effects on the drag due to lift are presented in figure 10 for both spanwise positions of the thrust line. These results are presented as increments in ΔC_D from zero lift plotted against wing-lift coefficient (propeller lift not included). The results of figure 10 were obtained from the difference in power-on and power-off longitudinal force minus the increment at zero lift.

Photographs of the tuft grid (figs. 25 and 26) indicate that the power-on wing-span load distribution may be appreciably different from the span loading with the propeller removed, particularly with the outboard-thrust location. Appreciable alteration of the span loading could have an important effect on the induced drag of the wing and it is therefore desirable to evaluate these possible slipstream effects with regard to airplane performance.

The results of figure 10 show no consistent trends with thrust coefficient for either location of the thrust line. It is apparent that changes in drag due to lift are fairly small at moderate lift coefficients and that the differences shown may be within the experimental accuracy. The absence of large drag increases throughout the lift range indicates that adverse slipstream effects on drag due to lift would not be expected to be appreciable for this configuration at subsonic speeds.

Downwash.- The variation of downwash angle with tail height obtained from the floating tails for the inboard- and outboard-thrust locations is presented in figures 13 and 14. Downwash angles with the propeller removed showed a consistent increase with angle of attack up to $\alpha = 8^\circ$. At the highest angle of attack with the propeller removed, the downwash angles decreased for some tail locations showing evidence of wing-root stall for both nacelle positions. This wing stall is also indicated in the tuft-grid photographs (figs. 25(a) and 26(b)). When the propeller was operating at the inboard location, the slipstream delayed flow separation and no evidence of root stall was apparent in the downwash data (fig. 13) or the tuft photographs (fig. 25(b)). This root stall was evident, however, for all power-on conditions for the outboard-thrust location (figs. 14 and 26(b)) where the slipstream did not intersect the stalled root sections.

Faired results from the data of figures 13 and 14 are presented in figures 15 and 16 to show the variation of downwash angle with thrust coefficient. Results for the inboard-thrust location (fig. 15) show generally consistent increases in downwash angle with thrust coefficient. It appears that the largest downwash changes due to power would be expected for a tail located above the wing-chord plane.

The nature of power effects on downwash for the outboard-thrust location (fig. 16) is considerably different from that for the inboard

position. The downwash angle at a given angle of attack was generally reduced by application of a small amount of power and the variation with thrust was fairly small above $T_c \approx 0.4$. These effects are probably due to some alteration of the wing-span loading by the slipstream since the major part of the slipstream did not intersect the tails. These possible span loading changes are also indicated in the tuft-grid photographs of figure 26 by alteration of the wing-tip vortex pattern when power was applied.

A comparison of downwash results obtained from the floating tails for the inboard-thrust location (fig. 15) and from tail-on force data (fig. 11) is presented in figure 17 for a tail located on the wing-chord plane ($h_t = 0$). Downwash angles obtained by both techniques are considered effective values and they are in very good agreement as regards the variation with angle of attack. A discrepancy of about 0.5° in the absolute value of the downwash angle is evident in two cases; a discrepancy which possibly is caused by some inaccuracies in the force data rather than in the floating tail results. The over-all agreement of $d\epsilon/d\alpha$ obtained by the two techniques and the consistent variation of ϵ at $\alpha = 0^\circ$ obtained from the floating-tail results attests the validity of downwash results obtained from the floating-tail surveys.

Dynamic pressure ratio.- The variation of local dynamic pressure ratio across the horizontal tail span is presented in figure 18. Results showing the effect of thrust coefficient (fig. 18(a)) were obtained from one floating tail located below the wing chord; whereas the data of figures 18(b) to 18(d) were obtained from the survey rakes mounted to the fuselage. These data were selected to illustrate typical results showing the effect of thrust coefficient, tail height, and angle of attack.

The results presented in figure 18(a) at $\alpha_g = 0^\circ$ show fairly consistent increases in q/q_0 with increasing T_c across the part of the tail immersed in the slipstream. Essentially all of the slipstream effects occur within the limits of the propeller which indicated that spreading of the jet was negligible. High peak values of q/q_0 occur at slightly less than 50 percent of the propeller radius (18 in. from root) and fall off abruptly outboard of this point (fig. 18(a)). This decrease is probably associated with both the propeller disk loading and the nacelle wake.

Local dynamic pressure ratios for several tail positions are presented in figure 18(b) for $\alpha = 0^\circ$ and $T_c = 2.09$. These data show an increase in dynamic pressure and the extent of the immersed span as the tail position moved into the slipstream. The maximum increase in q/q_0 occurred when the tail was located above the thrust line on the wing-chord plane ($h_t = 0$).

[redacted]

Effects of angle of attack on the dynamic pressure ratio at the tail are related to the tail location as a result of an upward displacement of the inclined slipstream relative to the tail. Figures 18(c) and 18(d) show results for tail positions above and below the thrust line at several angles of attack. It is apparent that the effect of angle of attack is reversed for the two tail locations presented. The high tail (h_t = 10) moved into the slipstream at high angles; whereas the slipstream center passed above the low tail (h_t = -15) at high angles of attack. Displacement of the inclined slipstream is shown in the tuft-grid photographs of figure 25(d) for a constant angle of attack with the thrust coefficient varied. The disturbed slipstream region at low thrust coefficients occurred relatively close to the wing and moved downward with increasing thrust approaching a straight extension of the thrust line.

Contours of dynamic pressure ratio for two thrust coefficients are presented in figure 19. These results were obtained from the rake surveys, part of which were presented in figure 18. Contours at an angle of attack of 0° for $T_c = 0.90$ and $T_c = 2.09$ indicate that the overall extent of the slipstream is not appreciably affected by thrust coefficient between the two values of T_c presented. Significant effects of thrust coefficient on the extent of the slipstream at an angle of attack are evident as a result of differences in slipstream deflection for the low and high slipstream velocities.

A simple method for estimating the dynamic pressure contours for any thrust coefficient and angle of attack is presented in appendix B and estimated results are compared with test results from the rake surveys.

Test data from the surveys indicate the actual dynamic pressure ratio at the horizontal tail; however, this information cannot necessarily be interpreted as indicating the lift effectiveness of a tail immersed in the slipstream. A comparison of tail lift effectiveness obtained from the surveys and from tail-on force data is presented in figure 20 for a tail located on the wing-chord plane. Lift effectiveness from the surveys was obtained from integration of local dynamic pressure ratios across the tail span and values from the force tests (fig. 11) were obtained from the ratio of $\partial C_m/\partial i_t$ to the maximum power-off value of $\partial C_m/\partial i_t$. The latter results represent the actual increase in lift effectiveness that was experienced by the tail immersed in the slipstream.

Substantial differences are evident for all power-on tests between results from the force tests and results from the surveys obtained from integrated values of q/q_o (fig. 20). These differences suggest that the lift effectiveness of the tail located in the slipstream was influenced by induced effects similar to those encountered at the wing. Although the

method of reference 3 for estimating increases in wing lift is not strictly applicable in determining R_t for this configuration, the fundamental considerations are the same and it is therefore of interest to evaluate results obtained by applying the concept used in reference 3. This concept assumes that the lift is proportional to the slipstream velocity ratio to the first power (that is, $\sqrt{q/q_o}$ rather than q/q_o) for conditions corresponding to a low aspect ratio of the part of the lifting surface immersed in the slipstream. Estimated results, based on the assumption that the tail lift effectiveness increased with $\sqrt{q/q_o}$, are in excellent agreement with force-test results throughout most of the angle-of-attack range (fig. 20). It should be pointed out, however, that the results of this investigation are limited with regard to prediction of the lift effectiveness of tails located at various positions in the propeller slipstream and more general research is needed to provide solutions to this problem.

Effects of Power on Over-All Stability and Trim

The foregoing discussion has been concerned with individual component effects contributing to complete airplane stability characteristics. Over-all effects of propeller operation for an assumed constant-power condition (fig. 5) are presented in figures 21, 22, and 23 for two positions of the horizontal tail. Pitching-moment results obtained from the faired curves of figures 11 and 12 with the center of gravity transferred to two different locations are presented in figure 21(a). The vertical location of the center of gravity was first transferred to the thrust line (solid lines) since the predominant adverse pitching-moment effects shown in figure 12 were due to the direct propeller thrust moment. The power-on results were also transferred to a center-of-gravity location $0.15\bar{c}$ below the thrust line to illustrate further effects of vertical location of the center of gravity. The longitudinal location of the center of gravity was selected to afford 15 percent $\bar{c}$ positive static margin for the power-off configuration (center of gravity at 35.8-percent $\bar{c}$). Results presented in figure 21(b) for the high tail position were obtained by adding the tail contribution determined from the downwash surveys to the tail-off results of figure 21(a). A dynamic pressure ratio of unity was considered applicable since the high tail (h_t = 20) was not immersed in the slipstream.

Effects of power on trim and stability characteristics are summarized in figures 22 and 23. Stabilizer setting for trim is plotted against airspeed in figure 22 for an assumed wing loading of 50 pounds per square foot at sea-level altitude. Power effects with the center of gravity on the thrust line were comparatively small for the configuration having the tail on the wing-chord plane (figs. 22(a) and 23); whereas large adverse

effects of power were encountered when the tail was raised to the high position (figs. 22(b) and 23). The downwash results of figure 15 indicate that adverse downwash effects with power were not vastly different for the two tail positions, therefore, the large effect of tail height with power on is primarily associated with a reduction in tail effectiveness due to moving the tail out of the slipstream. Adverse changes in downwash gradient due to power for the $h_t = 0$ configuration were counteracted by the stabilizing effects of increased q/q_o and $\frac{\partial q/q_o}{\partial C_L}$ in the slipstream and these favorable effects were not present for the high tail.

The pitching-moment data were transferred $0.15\bar{c}$ below the thrust line in order to utilize a favorable direct thrust effect in counteracting downwash changes due to power with the high tail. Effects of power on the trim and stability characteristics (figs. 22(b) and 23) for the $h_t = 20$ configuration were greatly reduced by placing the center of gravity below the thrust line and very small trim changes due to power occurred throughout the speed range.

The results of figures 22 and 23 are limited in general application; however, some important considerations relative to location of the horizontal tail and airplane center of gravity are indicated. The relationships presented in figure 23 summarize the large over-all effects of these two design variables for the model configuration tested. It is apparent that configurations having minimum power effects with flaps retracted can be attained for a wide range of tail heights by proper utilization of the direct propeller thrust moment to provide stability.

Tuft-Grid Flow Surveys

A pictorial drawing of the tuft grid and model is presented in figure 24 as an aid in interpreting the tuft-grid photographs of figures 25 and 26. The drawing and photographs have been placed so that downwash and sidewash angles are indicated by the vertical and horizontal projections of the tufts. Undisturbed flow regions near the center of the photographs are indicated by the tufts appearing as points. The apparent flow angularity near the edges of the grid is caused by parallax due to location of the camera relatively close to the grid. The camera was placed slightly outboard of the center of the grid and the actual spanwise location of the projection of the thrust line on the grid is inboard approximately 2 inches from the apparent location. It should be pointed out that the photographs of the grid present an instantaneous observation and they are limited for purposes of analysis, especially in those cases in which random transient fluctuations of flow are present.

Photographs of the tuft grid and the model with the propeller removed are presented in figure 25(a). The flow indicated for an angle of attack of 0° may be used as a reference for comparison inasmuch as essentially all of the apparent angularity is due to parallax. As the angle of attack was increased, the tip vortex flow became evident. At $\alpha = 10°$ evidence of wing-root stall was indicated and the separated flow region over the wing progressed outboard with further increases in angle of attack.

The flow behind the model with the propeller operating at $T_c = 2.09$ (fig. 25(b)) indicated that the slipstream effected discernible alteration of the basic flow over the wing at high angles of attack. The most apparent effects were alleviation of separation near the wing root and an upward displacement of the tip vortex. Irregularities near the wing at low angles of attack are associated with turbulence near the slipstream boundaries, and this disturbed region was displaced downward as the angle of attack was increased. A relatively smooth region of high downwash is seen in the center of the slipstream at $\alpha = 12°$.

Effects of increasing the slipstream velocity at a constant angle of attack are shown in figures 25(c), 25(d), and 26 for the inboard- and outboard-thrust locations. Downward movement of the disturbed slipstream region with increasing thrust is evident for all conditions. With the inboard-thrust location at $\alpha = 10°$ and $\alpha = 14°$ (figs. 25(c) and 25(d)) the severity of separation near the fuselage was reduced for all propeller-on conditions. No consistent effects of the slipstream are evident for the separation outboard of the nacelle at $\alpha = 14°$ (fig. 25(d)).

The salient slipstream effects with the thrust line located in the outboard location were associated with the tip vortex (fig. 26). Application of power generally raised the tip vortex, caused an inboard movement of the vortex center, and increased the extent of the vortex flow. These results suggest that significant changes in span loading were effected by the slipstream with the thrust line in the outboard position.

CONCLUSIONS

The results of a low-speed investigation of the effects of dual-rotation propeller operation on a semispan powered model with flaps retracted indicated the following conclusions:

1. Stability and trim changes associated with an extreme constant-power condition were found to be greatly dependent upon both tail height and vertical location of the center of gravity. Large adverse effects of power were obtained for a configuration having the center of gravity

located on the thrust line and the tail in a high position. It was found that adverse power effects could be essentially eliminated either by moving the tail down into the slipstream or by utilization of the direct propeller thrust moment associated with a vertical displacement of the center of gravity to provide stability.

2. The lift effectiveness of the tail located in the propeller slipstream was found to increase with the slipstream velocity ratio to the first power rather than to increase directly with the dynamic pressure ratio.

3. Lift-curve slopes of the complete model increased with thrust up to the highest thrust coefficient tested. The increment of wing-lift slope due to power reached a maximum near a thrust coefficient of unity and decreased thereafter. At the highest thrust coefficient investigated, about 90 percent of the lift-slope increase of the complete model was associated with the direct propeller forces.

4. Power-on downwash angles showed fairly consistent increases with thrust coefficient when the thrust line was located at one-third of the wing semispan; whereas results obtained with the propeller at the mid-semispan showed only small changes in downwash angle due to power and did not vary appreciably with thrust coefficient.

Langley Aeronautical Laboratory
National Advisory Committee for Aeronautics
Langley Field, Va.

APPENDIX A

COMPUTATION OF JET-BOUNDARY CORRECTIONS

Jet-boundary-induced-upwash velocities behind reflection-plane models mounted vertically in 7- by 10-foot, closed, rectangular wind tunnels were calculated by the method of images (see reference 5). The effect of 168 image tunnels has been summed and the results are presented in figures 27 and 28. Jet-boundary corrections applied to the tail-on pitching-moment data and the downwash angles from the surveys are as follows:

$$\Delta C_m = -57.3\left(\frac{\delta_T}{q/q_o} - \delta_W\right)\frac{S}{C}\frac{\partial C_m}{\partial i_t} C_{L_W}$$

$$\Delta\epsilon = 57.3\left(\frac{\delta_T}{q/q_o}\right)\frac{S}{C} C_{L_W}$$

where

$\delta_T = \frac{2C}{4s}\left(\frac{W}{\Gamma} + \frac{\Delta W}{\Gamma}\right)$, $\frac{W}{\Gamma}$ and $\frac{\Delta W}{\Gamma}$ obtained for desired location above or below the wing

δ_W jet-boundary correction factor at wing from reference 2 (0.131)

δ_T total correction factor at tail (0.196 used for all tail positions)

S semispan wing area (8.0 square feet)

C tunnel cross-sectional area (70 square feet)

s vortex semispan (5.4 feet)

W/Γ upwash velocity at lifting line for unit circulation from figure 27

$\Delta W/\Gamma$ additional upwash velocity behind lifting line for unit circulation from figure 28

C_{L_W} wing-lift coefficient (propeller lift component not included)

[redacted]

$\partial C_m/\partial i_t$ change in pitching moment per degree change in stabilizer setting determined from tail-on tests

q/q_o average dynamic pressure ratio at tail determined from integrated surveys

APPENDIX B

ESTIMATION OF DYNAMIC PRESSURE RATIO IN THE SLIPSTREAM

An empirical method for estimating the dynamic pressure ratio across the tail span for tails immersed in a slipstream has been derived from experimental results of this investigation. This estimation procedure is given in figure 29 for $T_c = 0.90$ at $\alpha = 0^\circ$. A horizontal tail located above the wing-chord plane ($h_t = 5$) is shown to illustrate the relationship between the projected propeller disk and the horizontal tail.

The rectangular distribution enclosed by the dashed lines represents the increment of dynamic pressure ratio in the slipstream based on actuator-disk-momentum theory. The maximum ordinate of the assumed trapezoidal distribution was obtained by equating areas of the assumed and rectangular distributions. Maximum values of $\Delta q/q_o$ for any thrust coefficient were obtained from the following relationship:

$$\left(\frac{\Delta q}{q_o}\right)_{max} = 3.91 T_c$$

where Δq is the increment of dynamic pressure in the slipstream from the free-stream value. Contours of dynamic-pressure ratio were obtained from the trapezoidal distribution by the addition:

$$\frac{q}{q_o} = 1.0 + \frac{\Delta q}{q_o}$$

A comparison of the estimated variation of local q/q_o across the tail span with values obtained from the rake surveys is presented in figure 30(a) for a number of tail positions at $\alpha = 0^\circ$. The agreement between estimated and test results is very good with regard to effects of tail position on the general shape of the curves and also the absolute magnitude of q/q_o with the exception of the $h_t = -5$ location.

Estimated results from figure 29 were considered directly applicable at $\alpha = 0^\circ$ only because of slipstream deflection with the thrust axis inclined. The complex nature of the flow behind the model imposes difficulties in predicting the slipstream displacement by theoretical methods, and an empirical approach has accordingly been used in an attempt to approximate this displacement at the tail. The slipstream displacement was obtained from the following relationships:

[redacted]

$$\Delta r = l_t \tan \alpha\left(1 - \frac{d\epsilon}{d\alpha}\right) \tag{1}$$

$$\frac{d\epsilon}{d\alpha} = \frac{d\epsilon_o}{d\alpha}\left(\frac{1}{1 + s}\right) + \frac{s}{1 + s} \tag{2}$$

where

Δr upward displacement of true slipstream center from the projected inclined thrust line

l_t tail length from wing $(\bar{c}/4)$

α inclination of thrust line

$d\epsilon_o/d\alpha$ wing downwash gradient, power off

$$1 + s = \sqrt{1 + \frac{8}{\pi} T_C}$$

Equations (1) and (2) have no strict theoretical justification but are based on a rational combination of first-order effects. Equation (2) was derived from a simple addition of the inclined slipstream velocity vector to the power-off vector.

Estimated results at several angles of attack are compared with test data in figures 30(b) and 30(c) for two thrust coefficients. The very good over-all agreement shown in figure 30 indicates that the approximate relationships presented herein afford a good estimation of the effects of tail height and angle of attack for a wide range of thrust coefficients for the model configuration investigated.

REFERENCES

1. Bird, John D., and Riley, Donald R.: Some Experiments on Visualization of Flow Fields Behind Low-Aspect-Ratio Wings by Means of a Tuft Grid. NACA TN 2674, 1952.

2. Polhamus, Edward C.: Jet-Boundary-Induced-Upwash Velocities for Swept Reflection-Plane Models Mounted Vertically in 7- by 10-Foot, Closed, Rectangular Wind Tunnels. NACA TN 1752, 1948.

3. Smelt, R., and Davies, H.: Estimation of Increase in Lift Due to Slipstream. R. & M. No. 1788, British A.R.C., 1937.

4. Ribner, Herbert S.: Notes on the Propeller and Slipstream in Relation to Stability. NACA ARR L4I12a, 1944.

5. Swanson, Robert S., and Schuldenfrei, Marvin J.: Jet-Boundary Corrections to the Downwash Behind Powered Models in Rectangular Wind Tunnels With Numerical Values for 7- by 10-Foot Closed Wind Tunnels. NACA ARR, Aug. 1942.

[redacted]

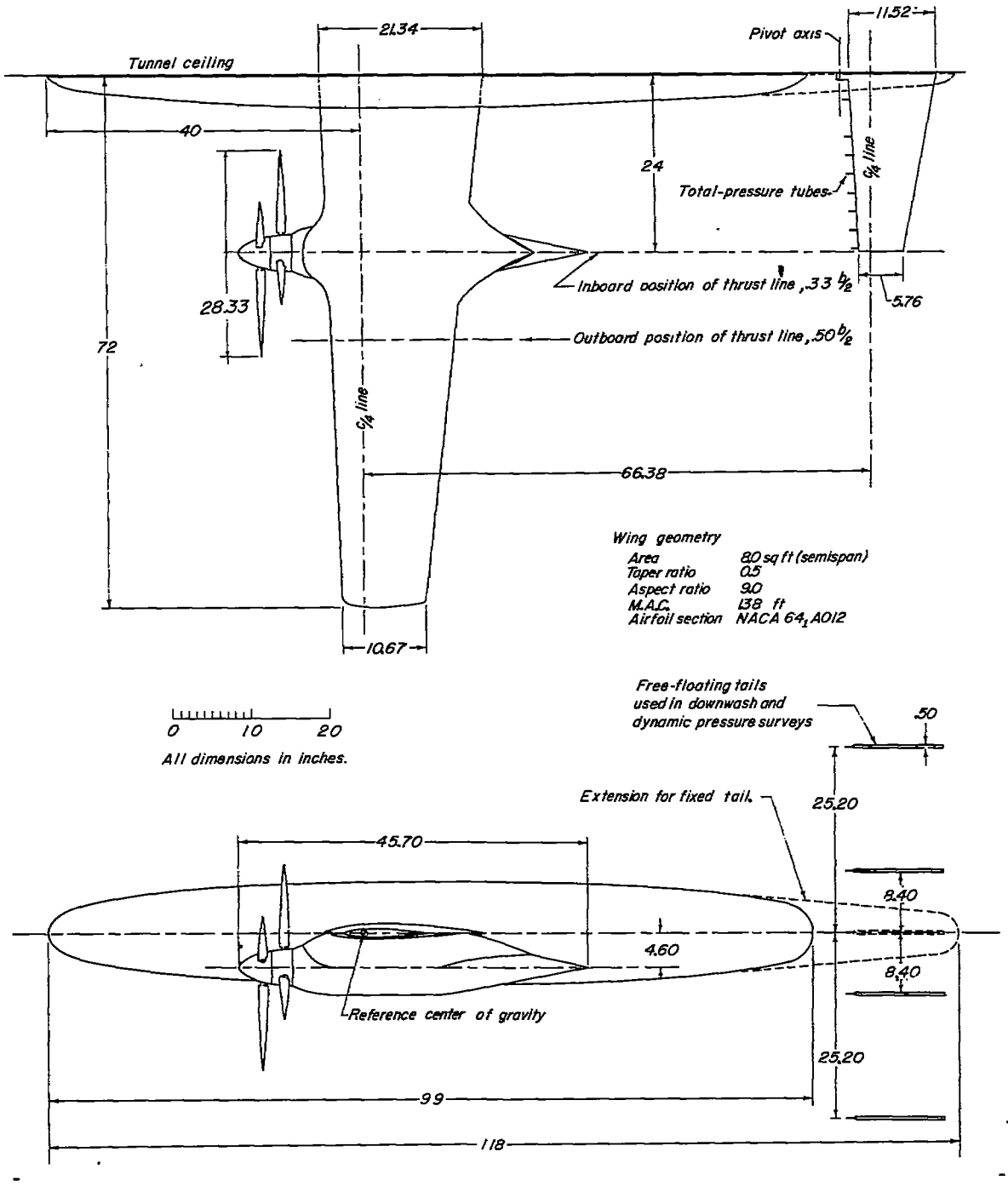

(a) General arrangement of model configuration.

Figure 1.- Drawings of the semispan powered model.

[redacted]

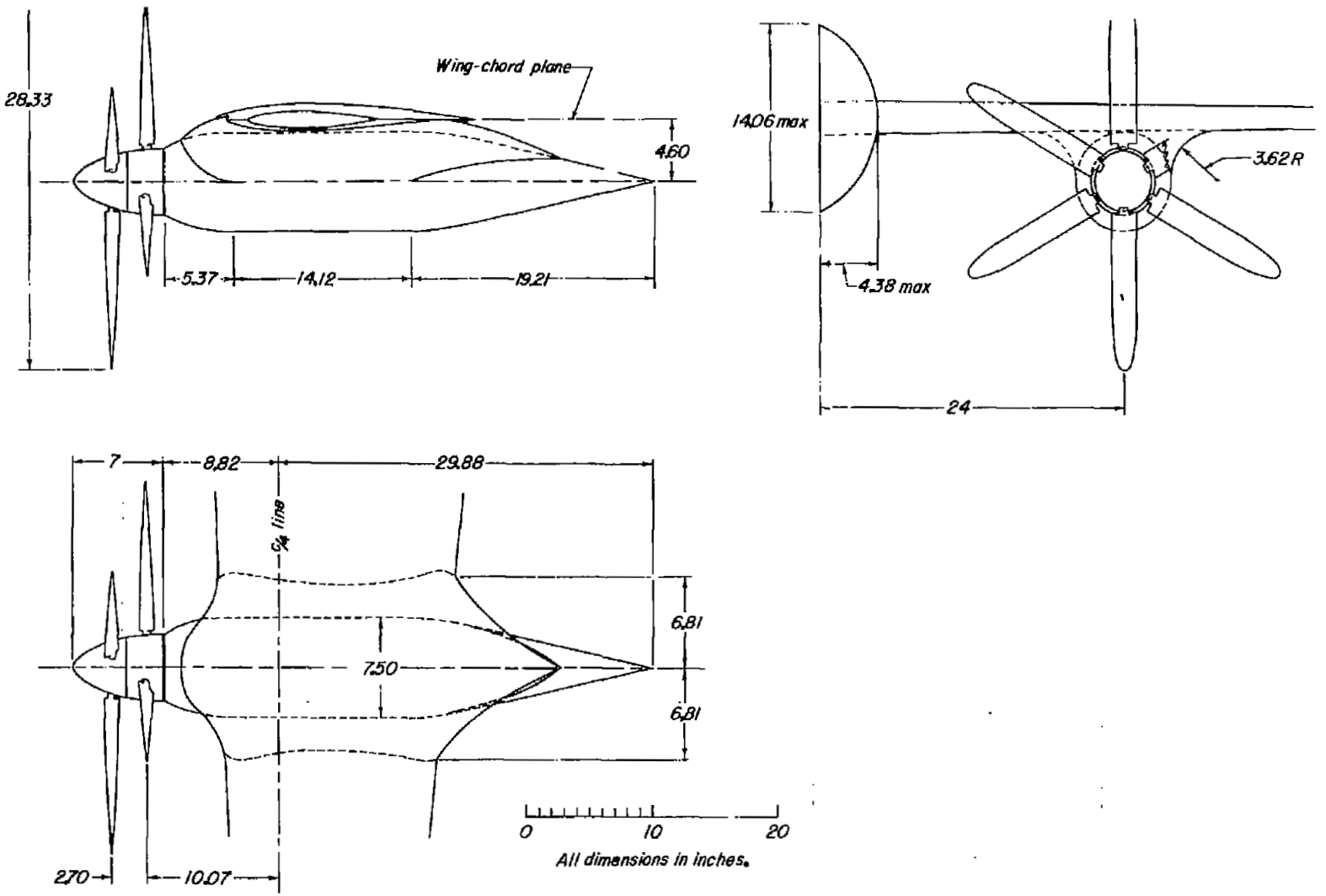

(b) Nacelle details.

Figure 1.- Concluded.

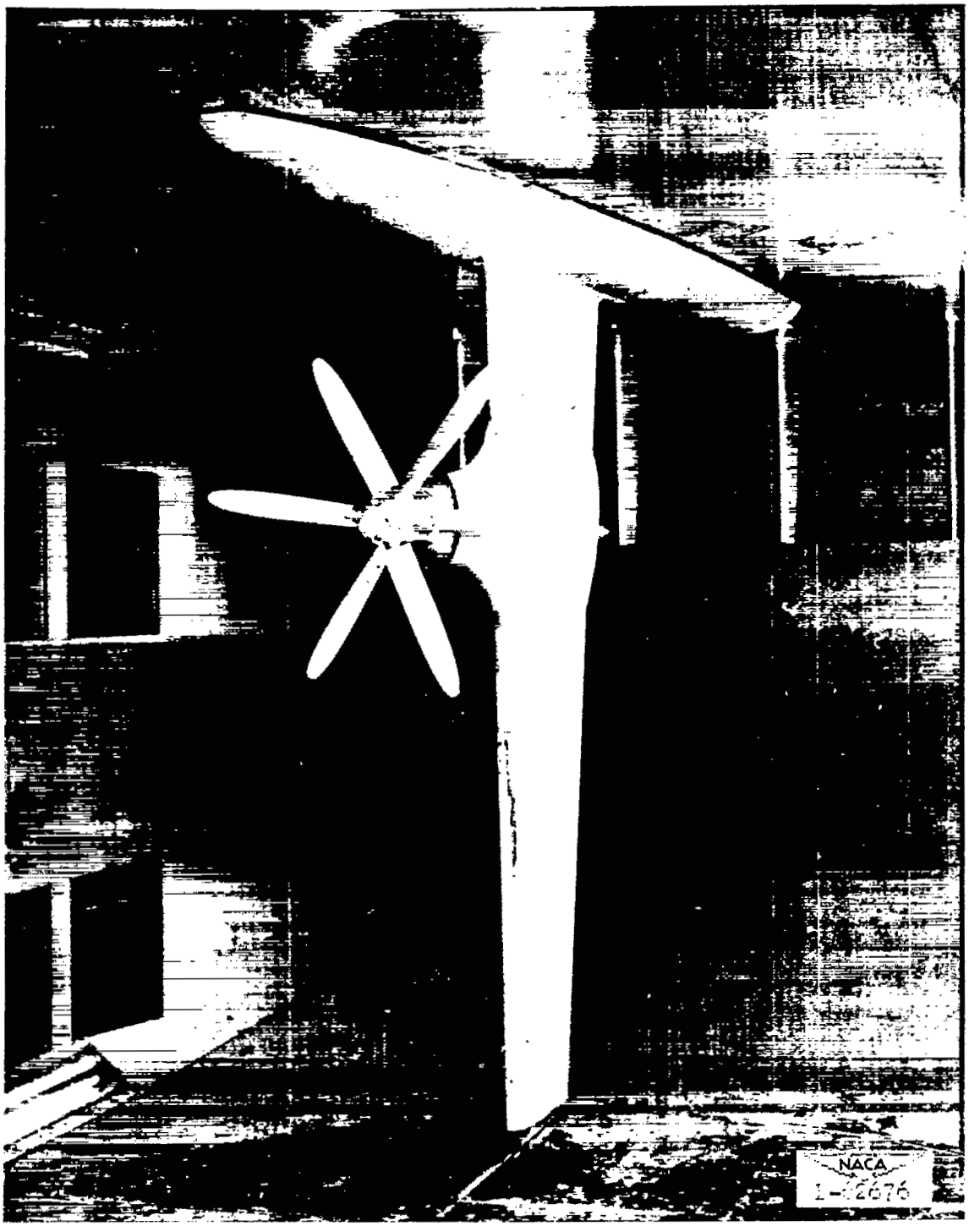

Figure 2.- Model mounted in the Langley 300 MPH 7- by 10-foot tunnel.

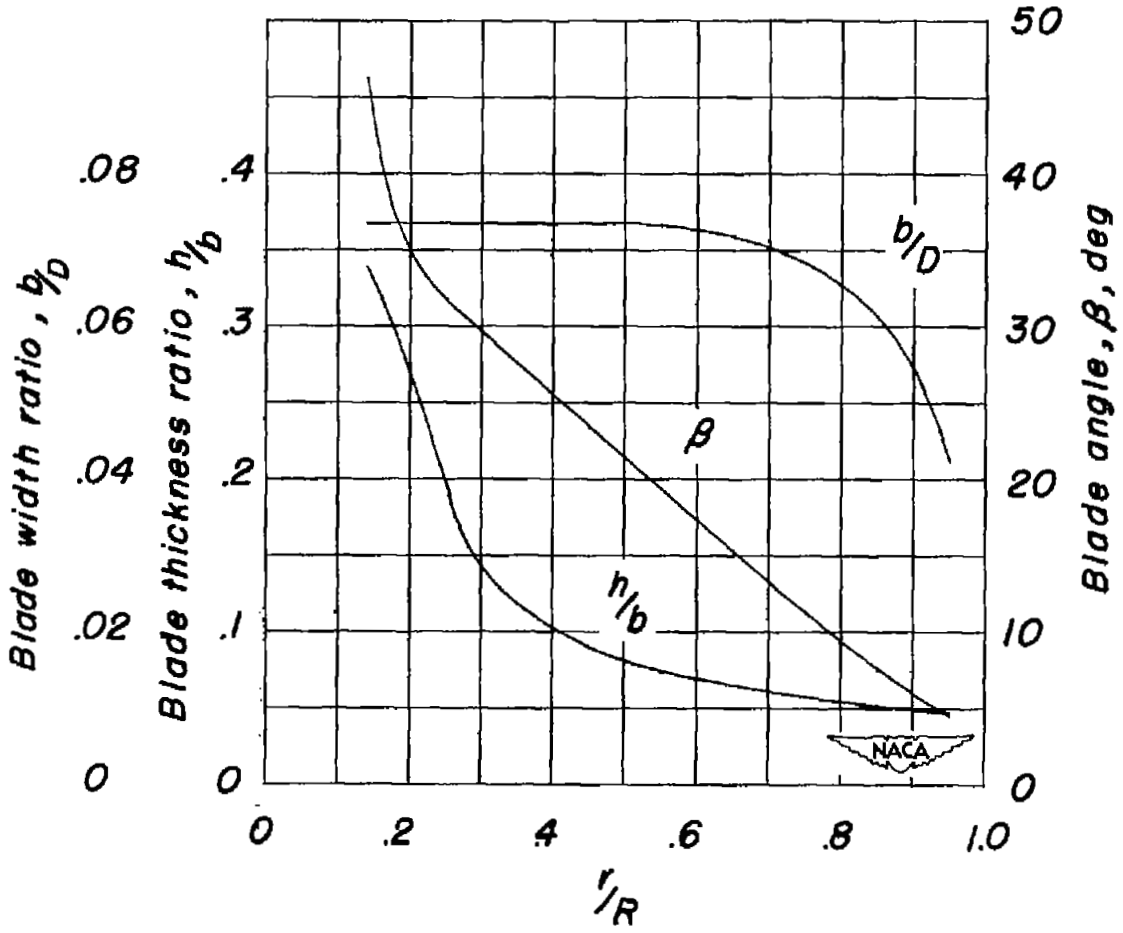

Figure 3.- Blade-form characteristics of the model propeller.

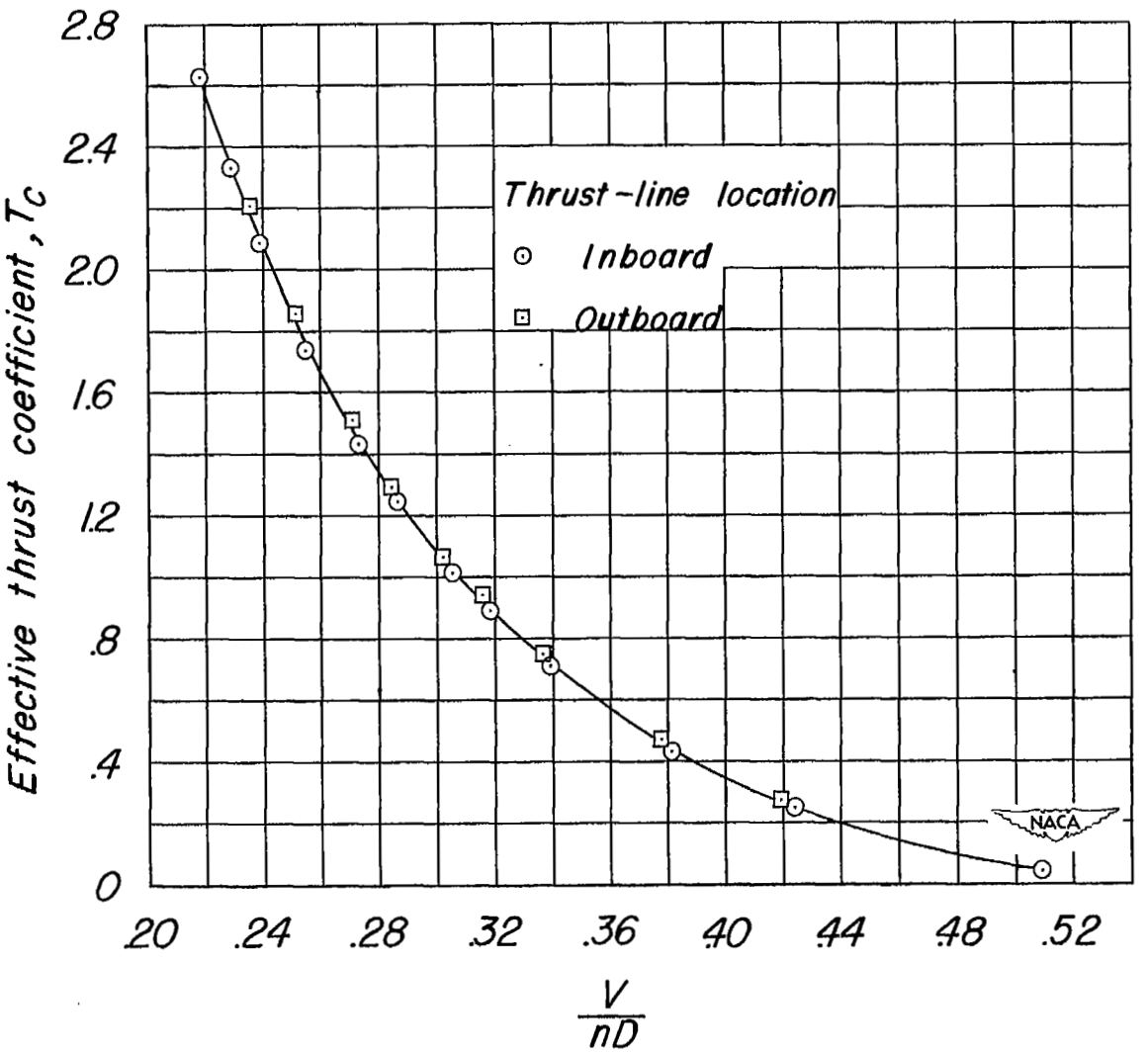

Figure 4.- Variation of effective thrust coefficient with propeller advance-diameter ratio.

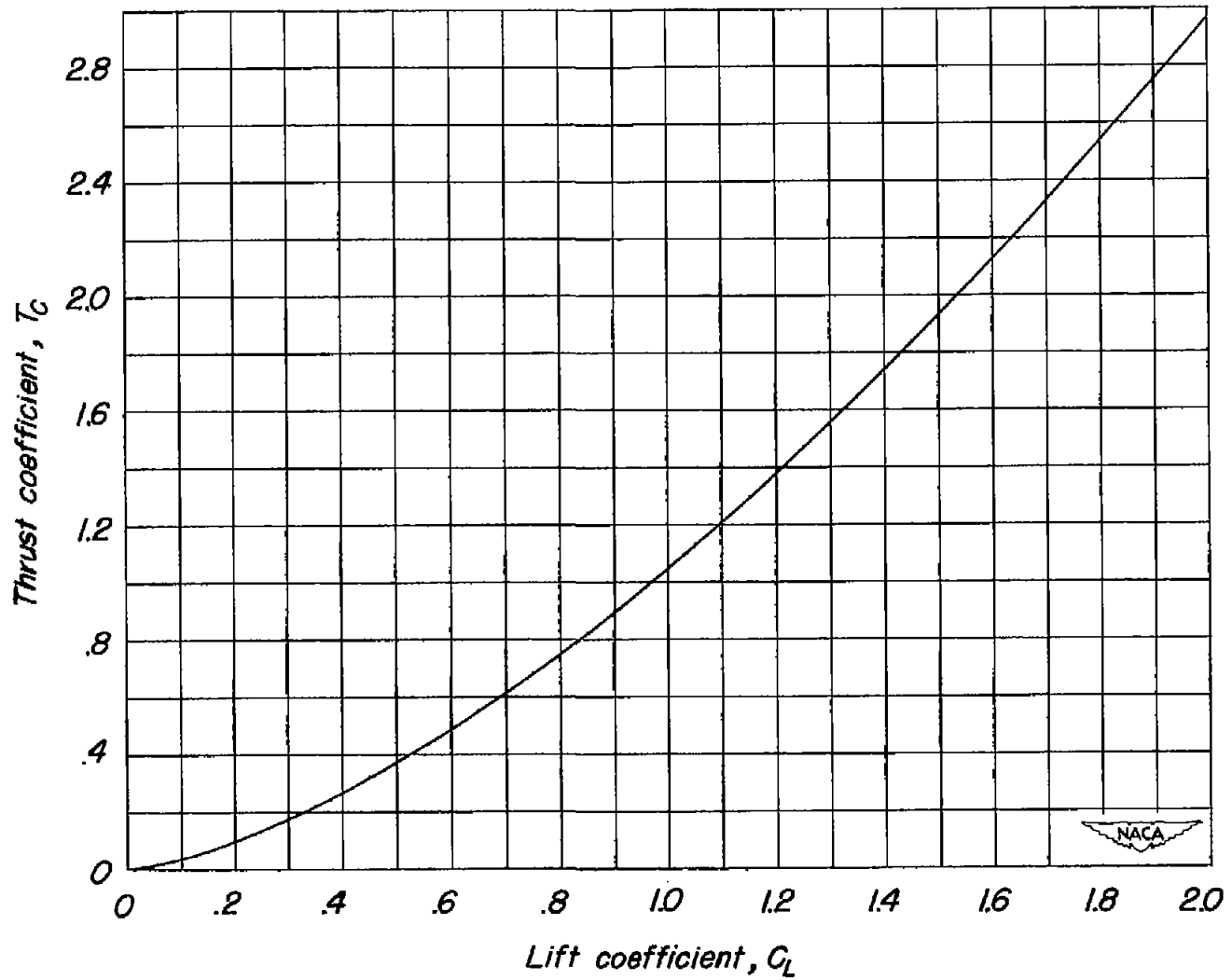

Figure 5.- Variation of thrust coefficient with lift coefficient for the assumed constant-power condition simulated in tail-on tests.

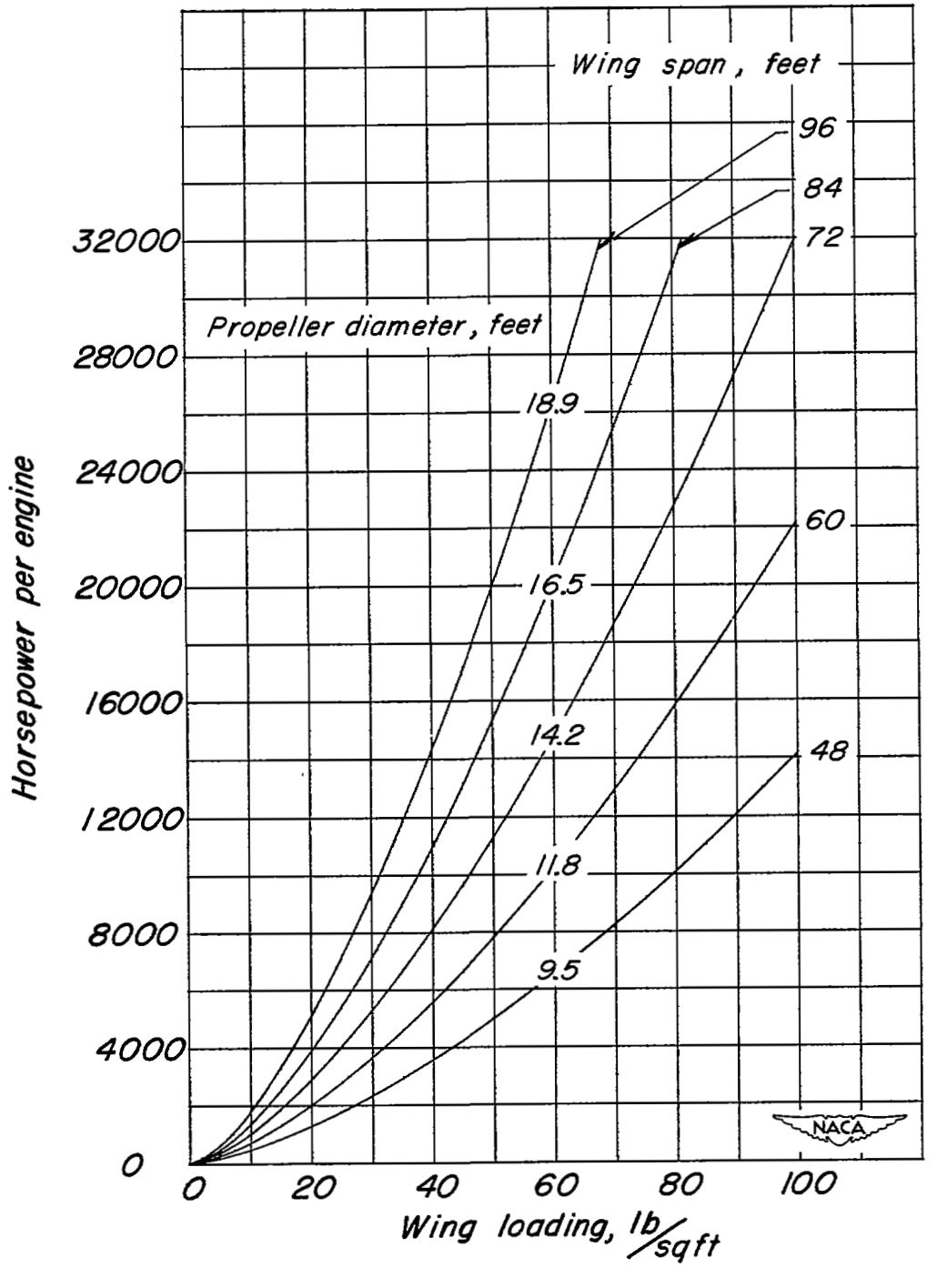

Figure 6.- Horsepower represented in the constant-power tests as a function of airplane wing loading and size.

[redacted]

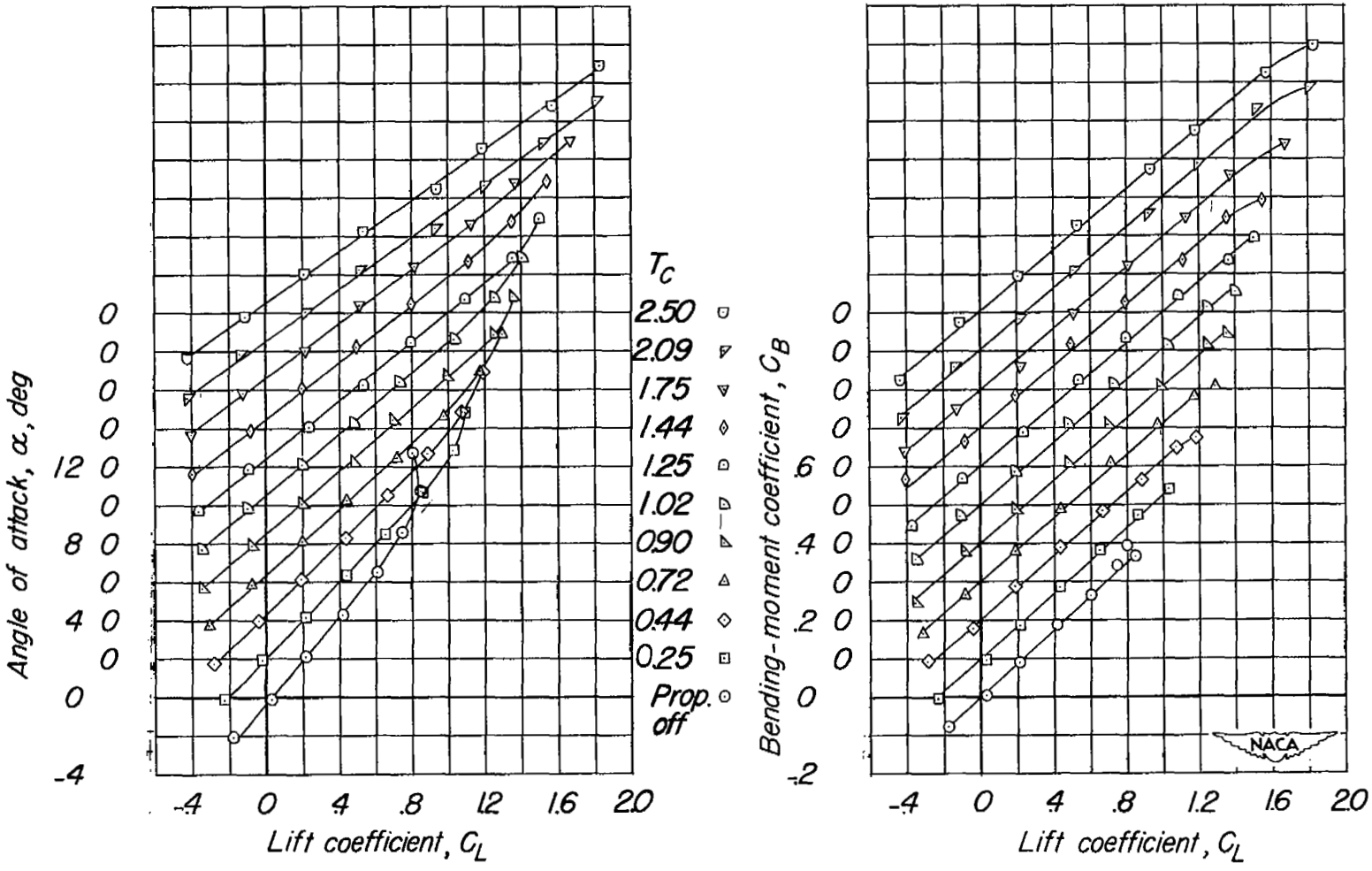

Figure 7.- Aerodynamic characteristics of the semispan powered model. Inboard-thrust location; horizontal tail off.

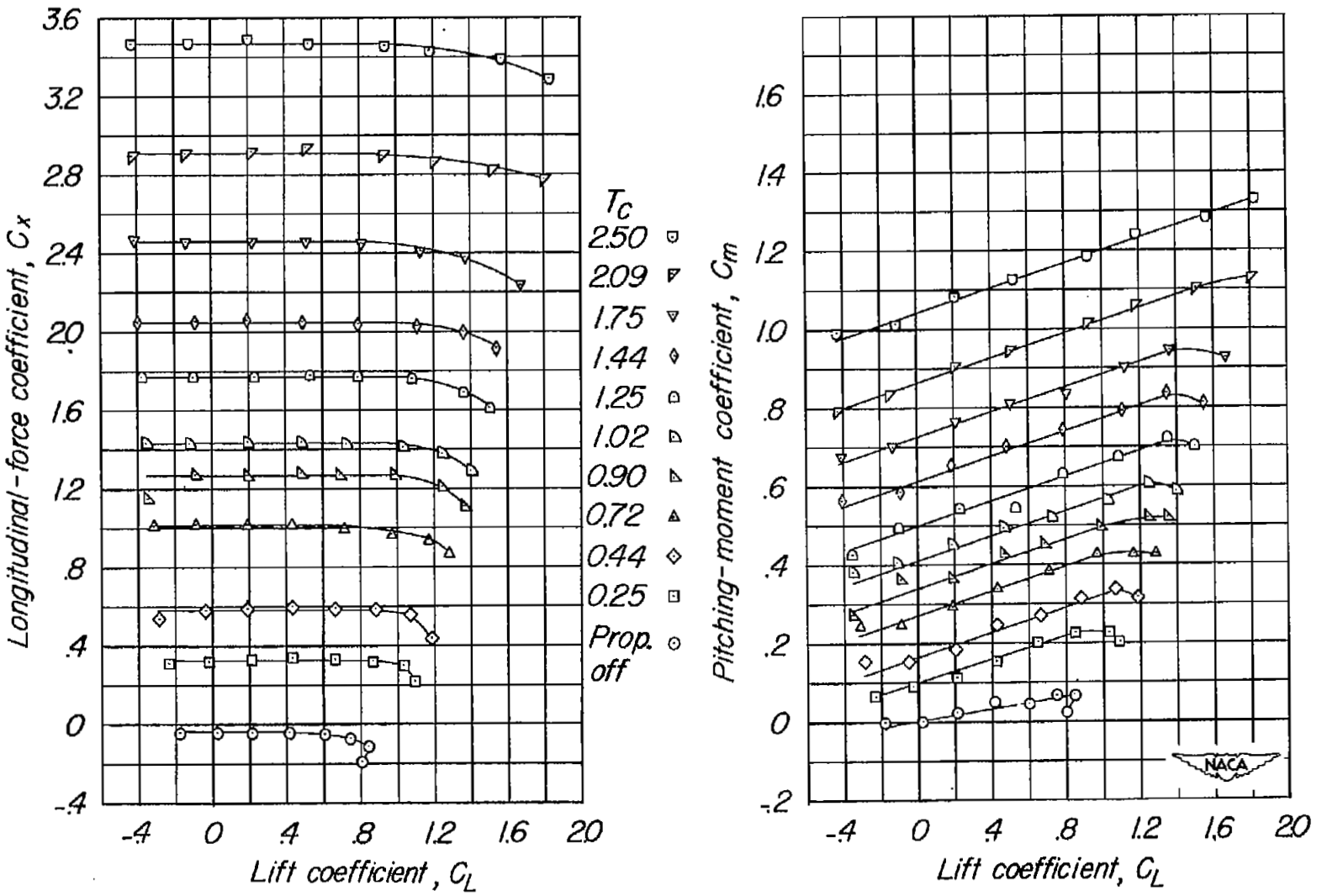

Figure 7.- Concluded.

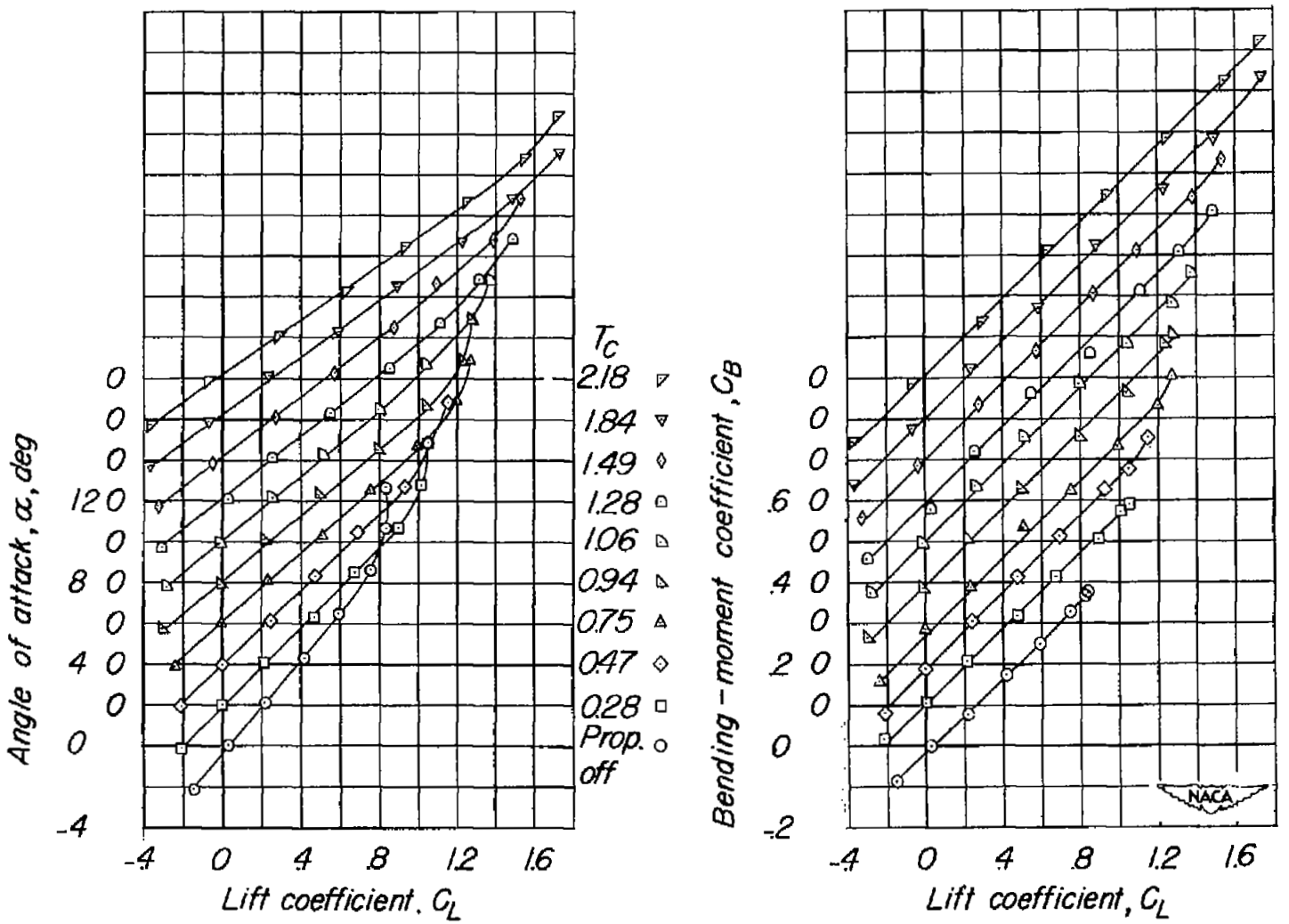

Figure 8.- Aerodynamic characteristics of the semispan powered model. Outboard-thrust location; horizontal tail off.

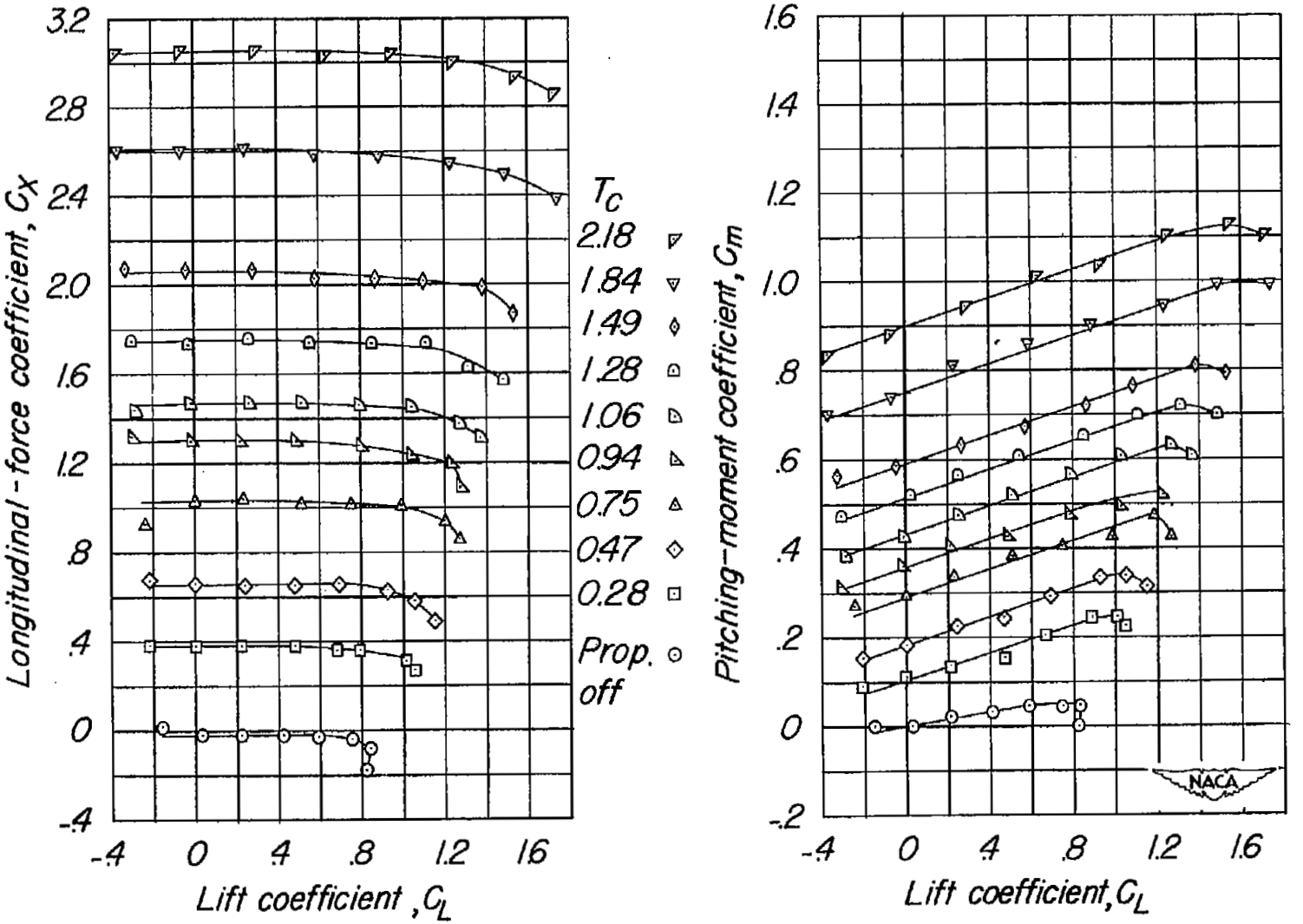

Figure 8.- Concluded.

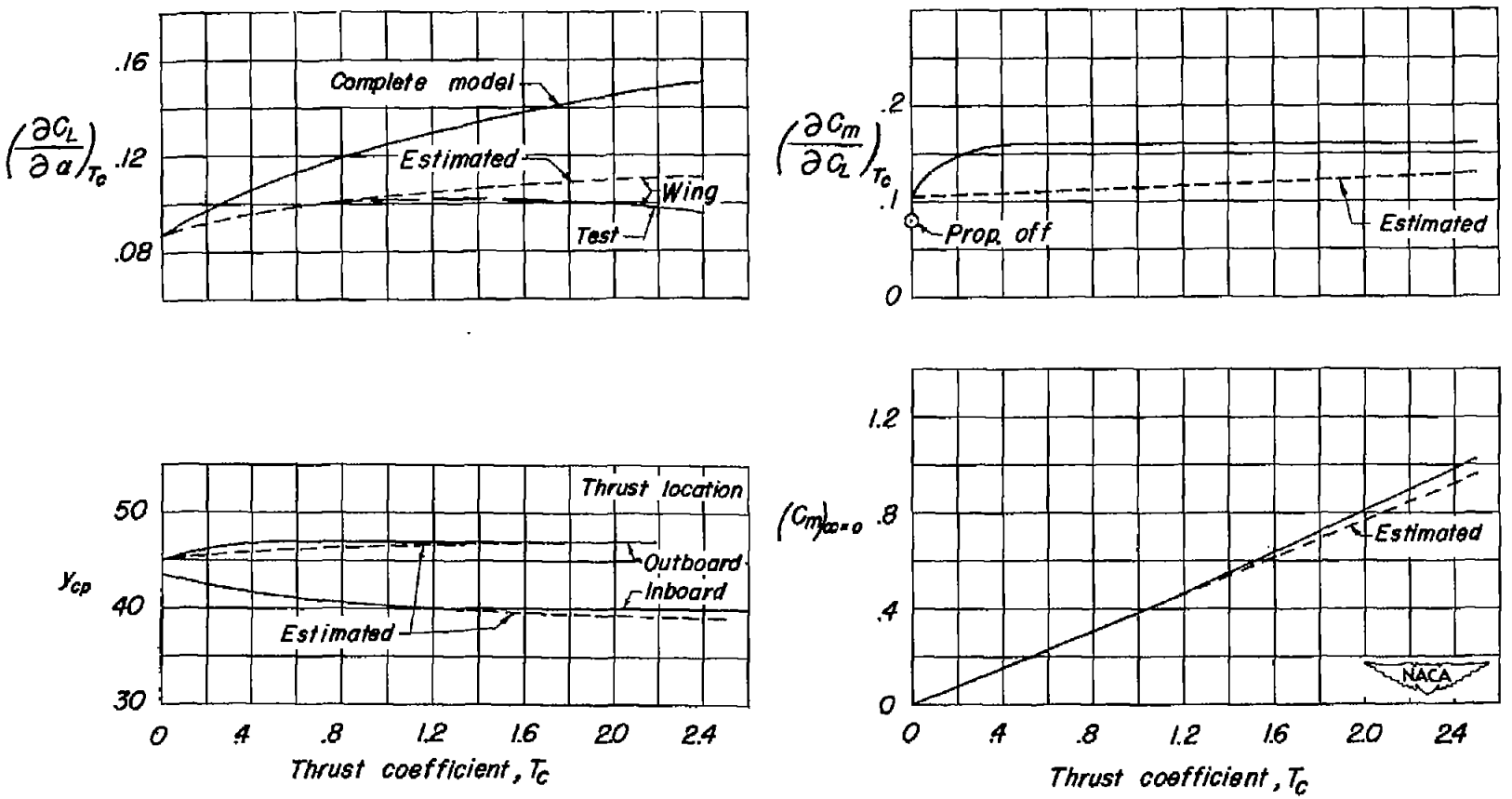

Figure 9.- Summary of tail-off aerodynamic characteristics of the semi-span powered model.

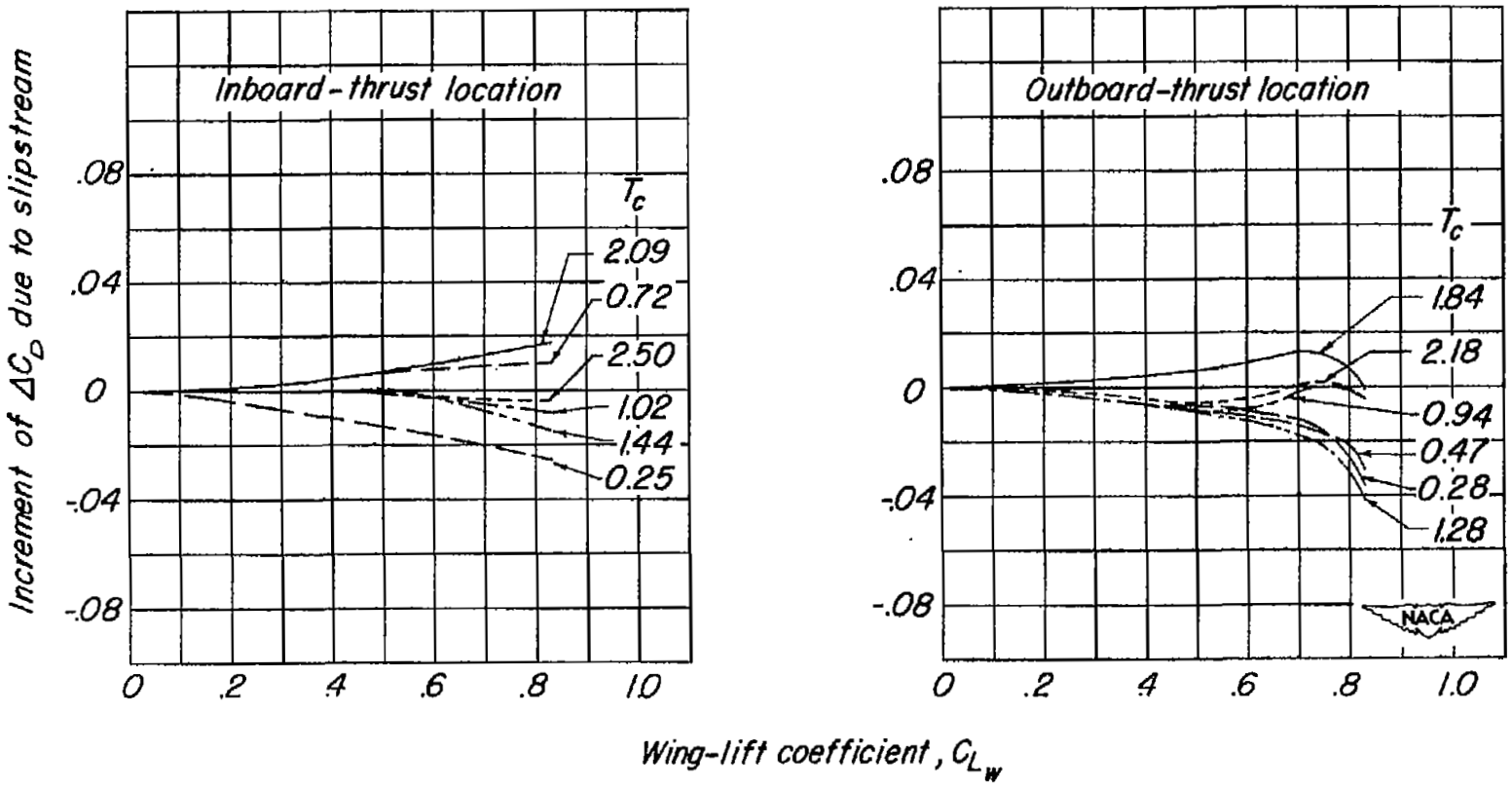

Figure 10.- Slipstream effects on drag due to lift. Horizontal tail off.

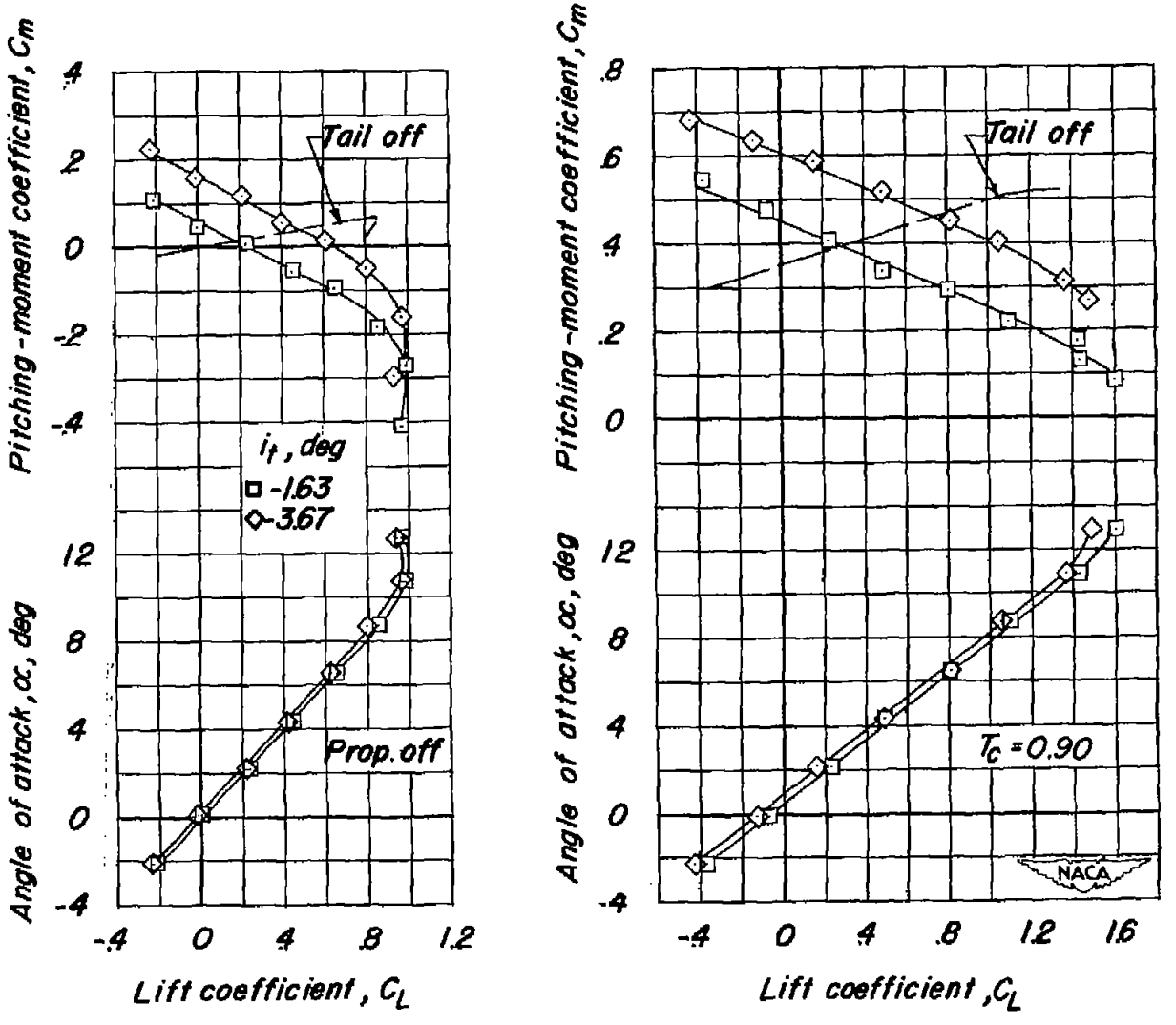

Figure 11.- Lift and pitching-moment characteristics of the semispan powered model obtained with a horizontal tail attached to the model. Constant thrust; $h_t = 0$; inboard-thrust location.

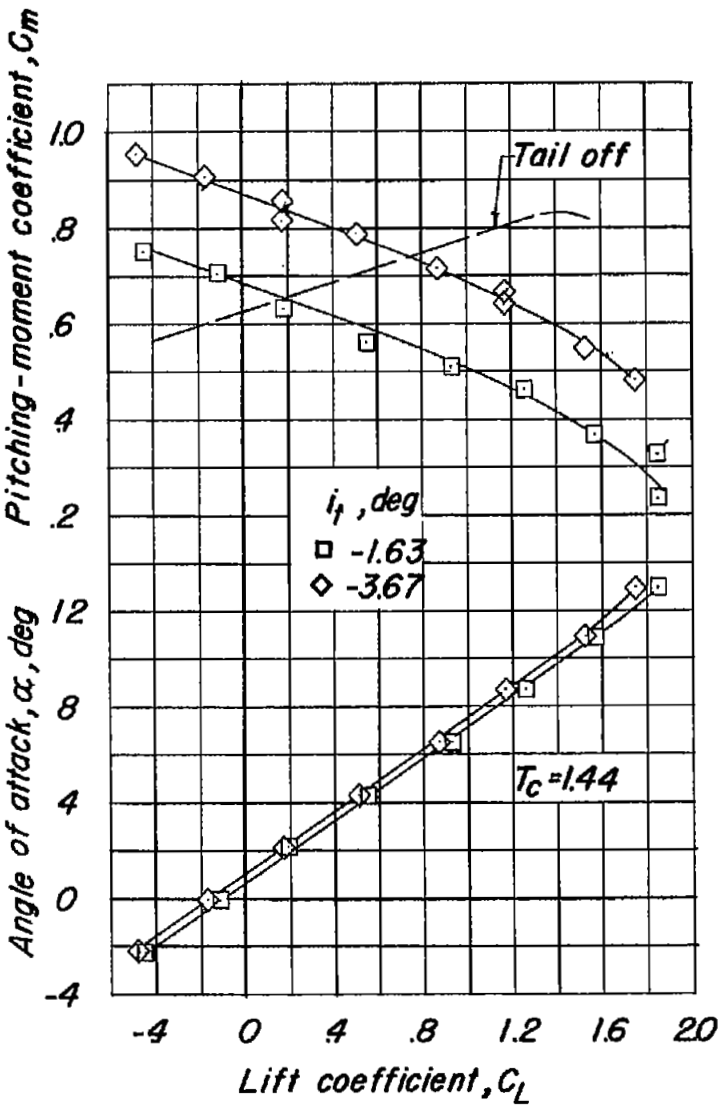

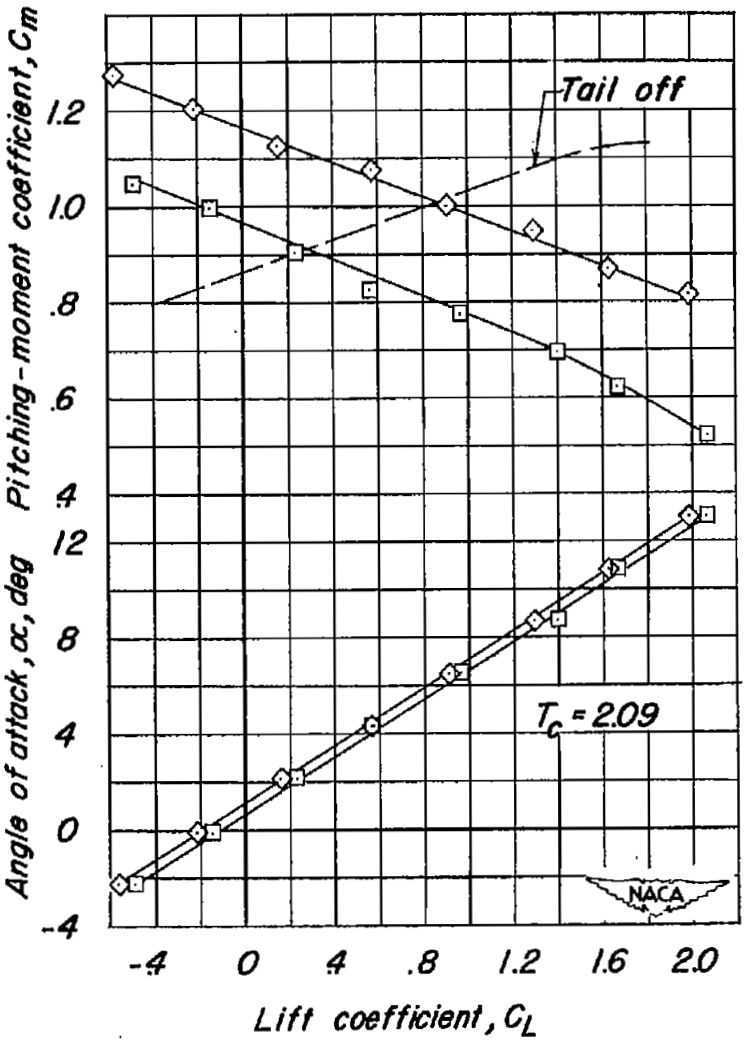

Figure 11.- Concluded.

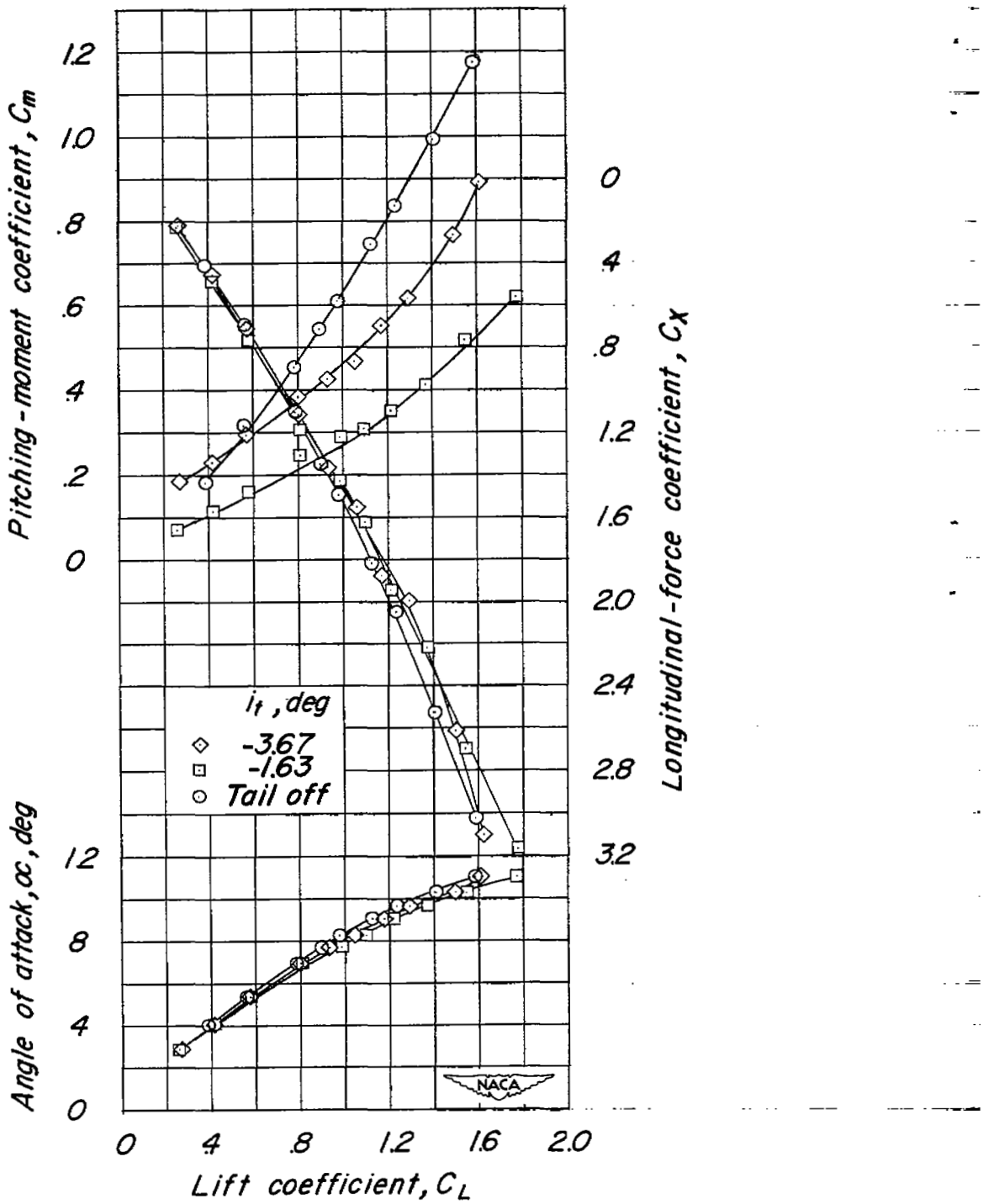

Figure 12.- Aerodynamic characteristics of the semispan powered model with and without a horizontal tail. Constant power; h_t = 0; inboard-thrust location.

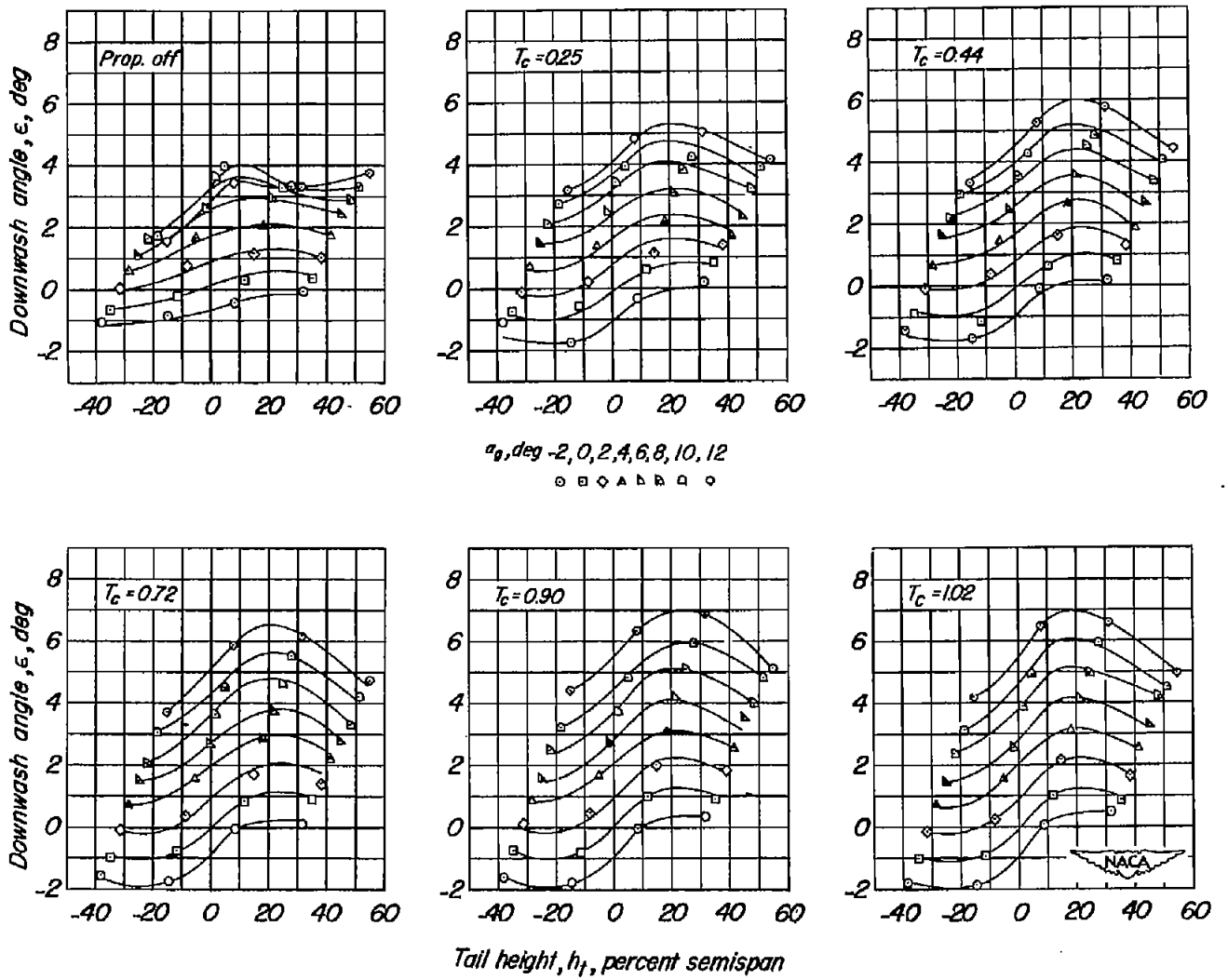

Figure 13.- Downwash angles obtained from floating tails. Inboard-thrust location.

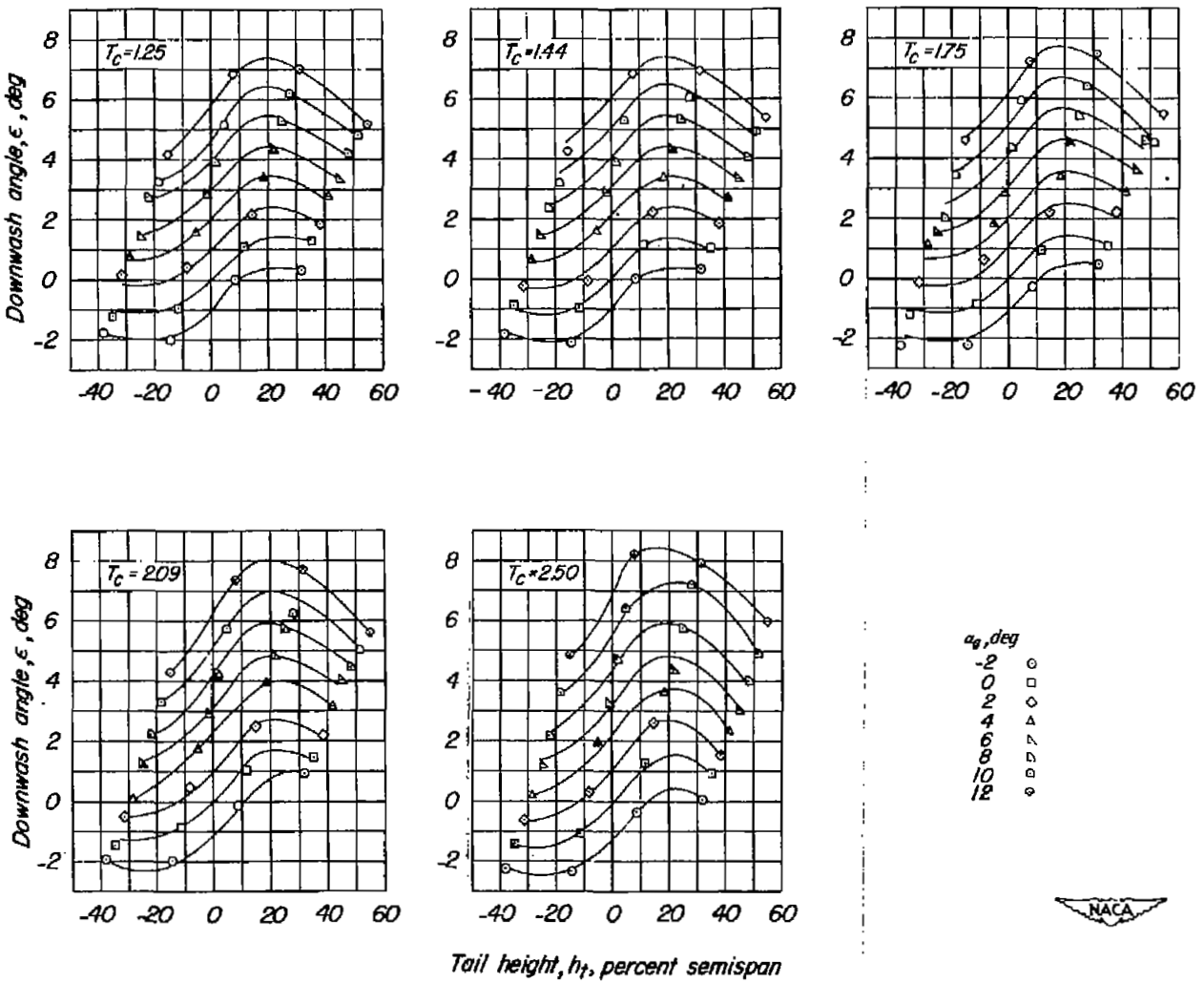

Figure 13.- Concluded.

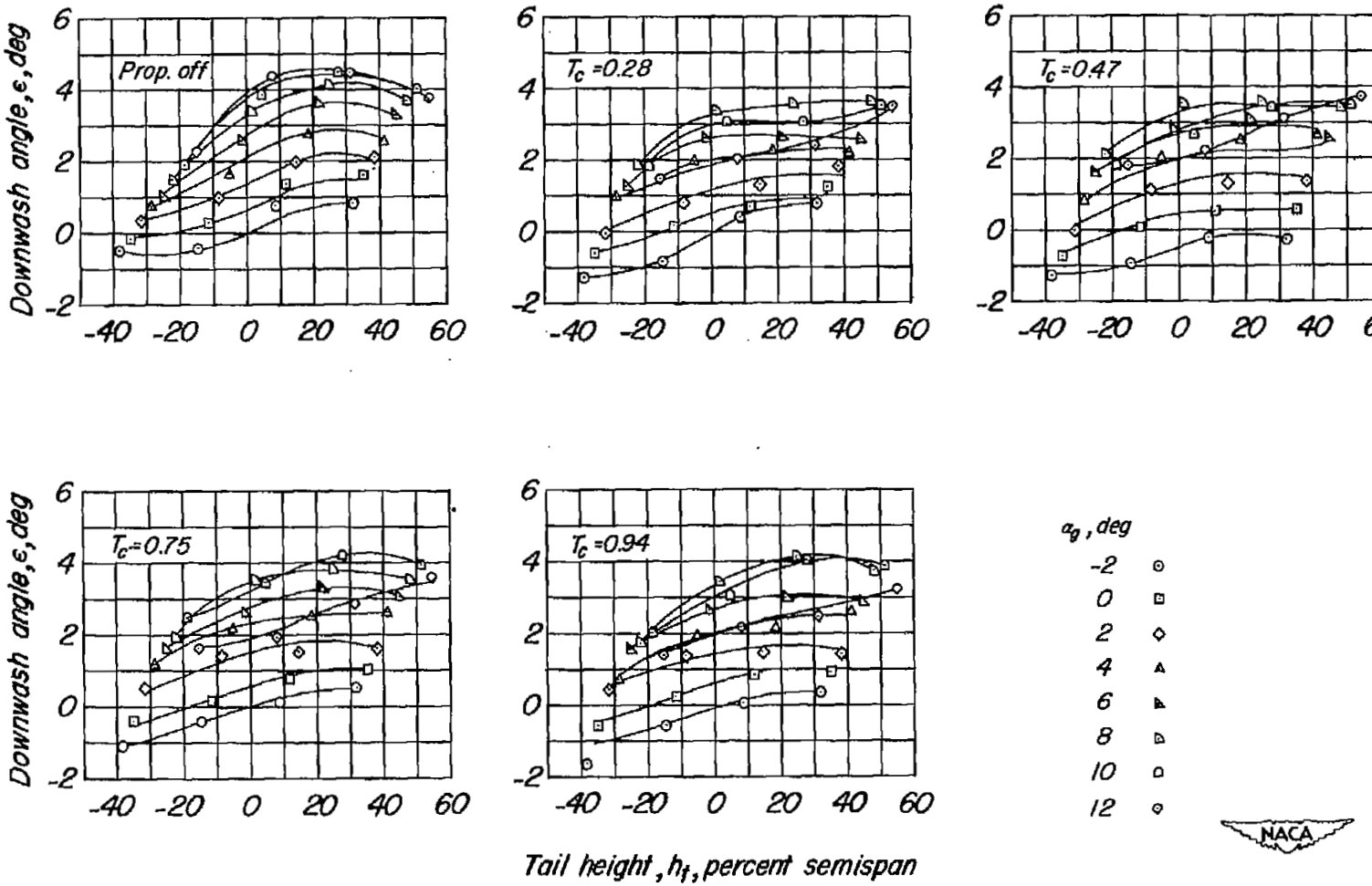

Figure 14.- Downwash angles obtained from floating tails. Outboard-thrust location.

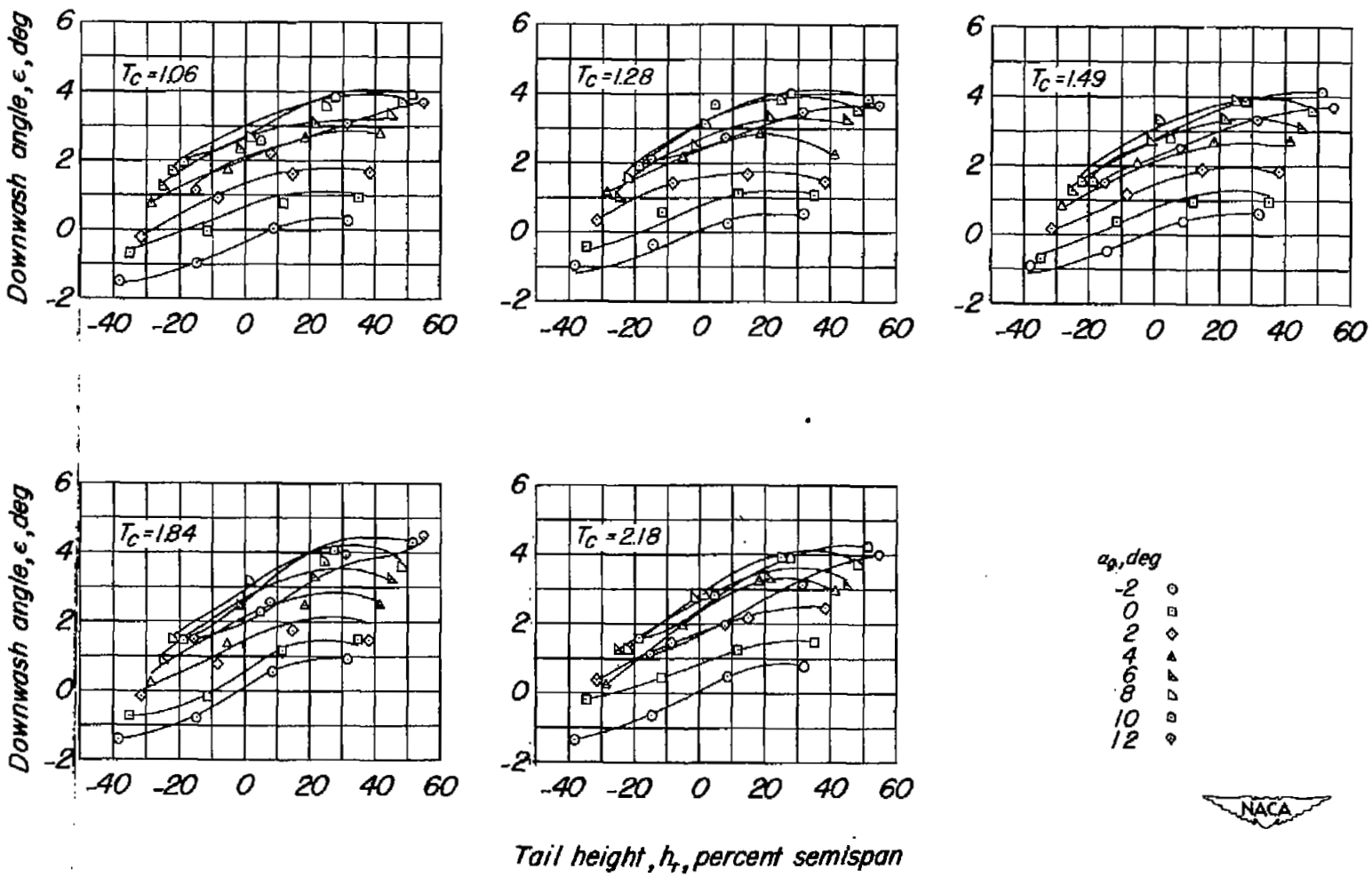

Figure 14.- Concluded.

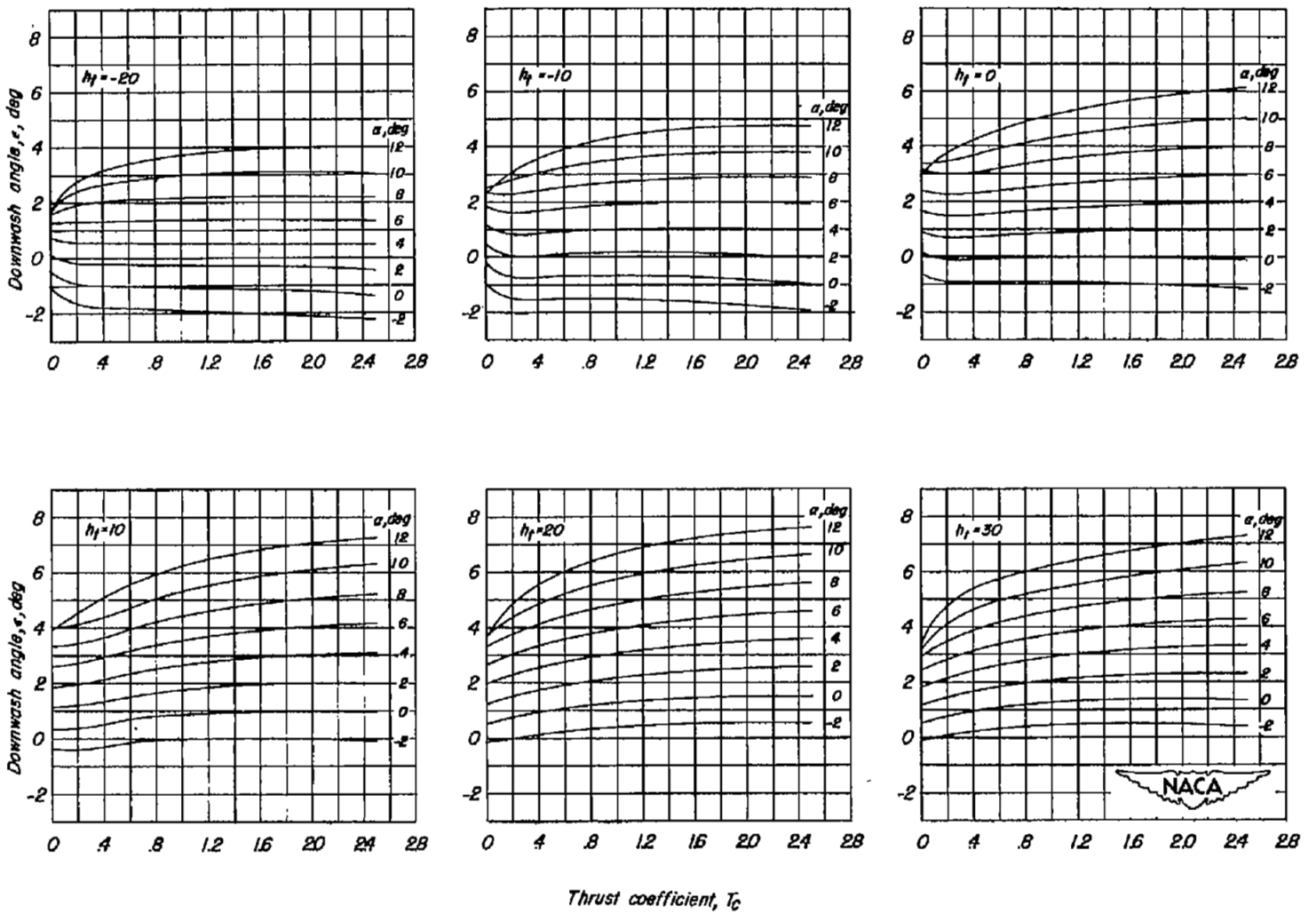

Figure 15.- Variation of downwash angle with thrust coefficient. Inboard-thrust location.

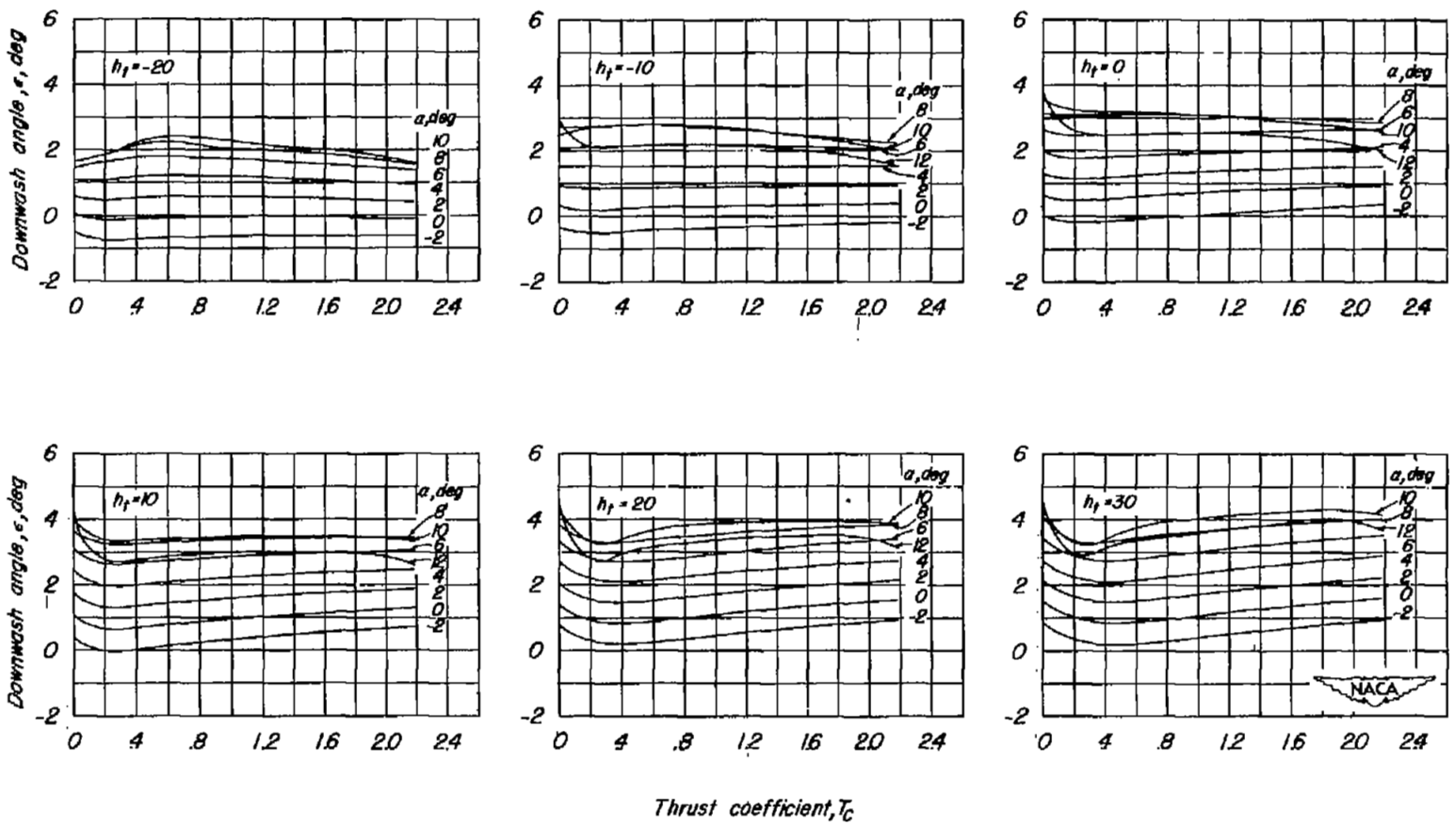

Figure 16.- Variation of downwash angle with thrust coefficient. Outboard-thrust location.

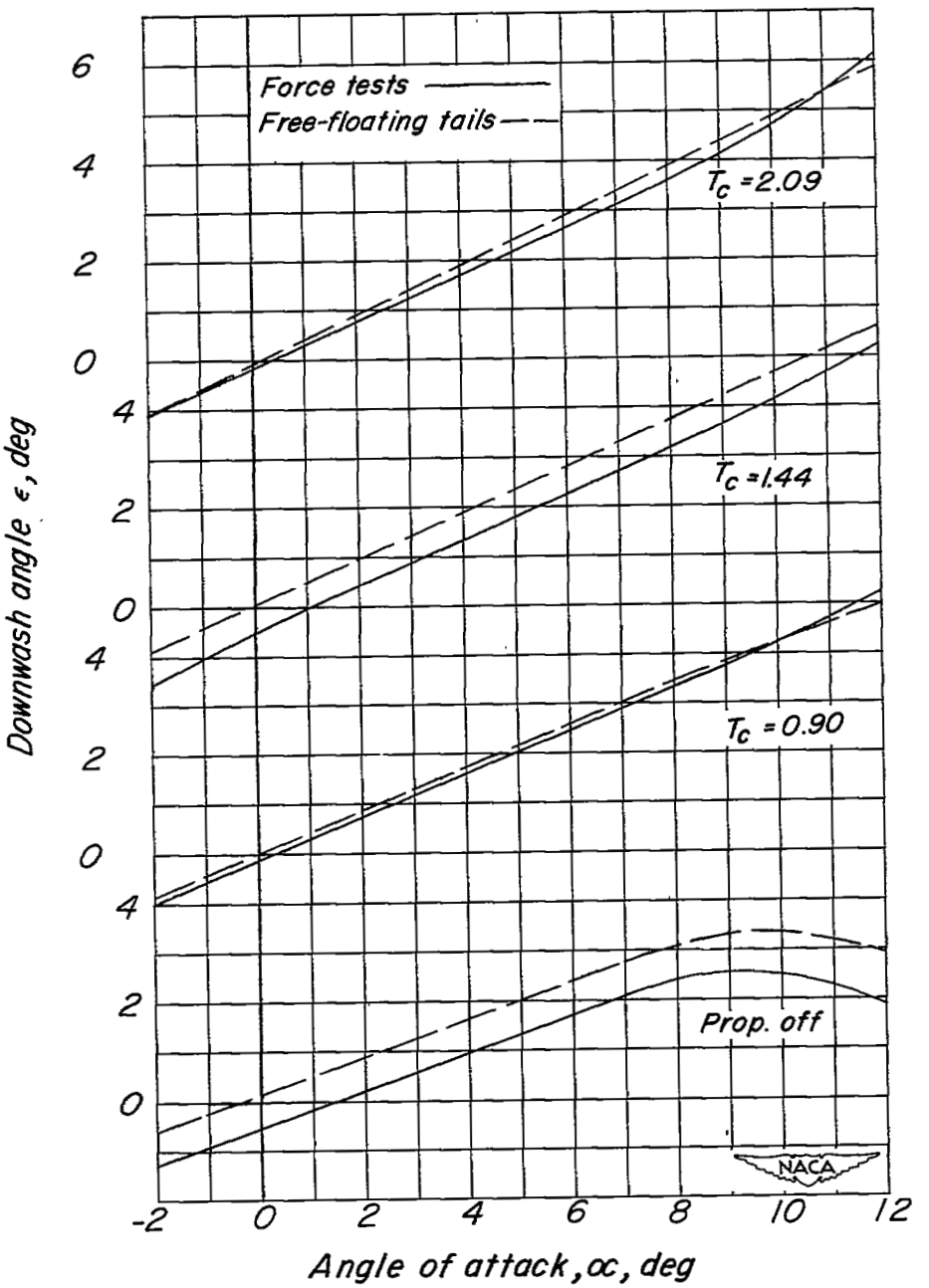

Figure 17.- Comparison of downwash angles obtained from the floating tails and from force tests. Inboard-thrust location; $h_t = 0$.

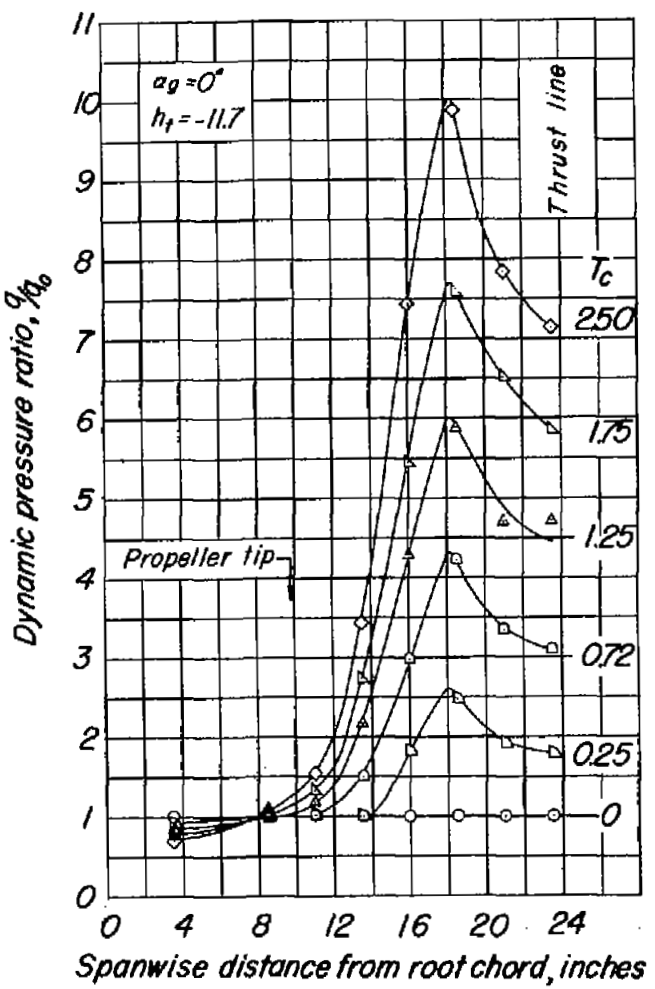

(a) Effect of thrust coefficient.

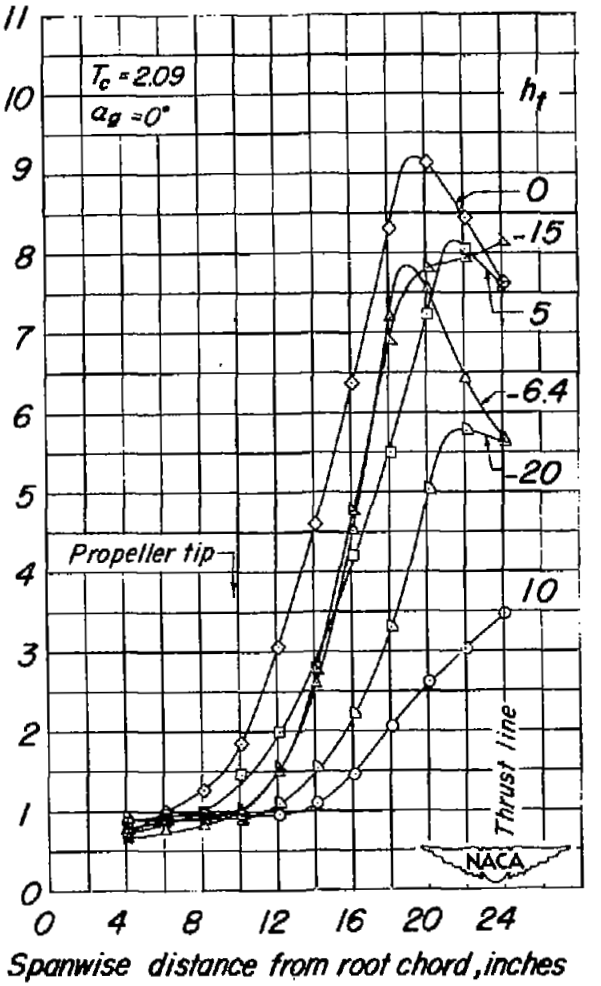

(b) Effect of tail height.

Figure 18.- Variation of local dynamic pressure ratio across the tail span obtained from surveys. Inboard-thrust location.

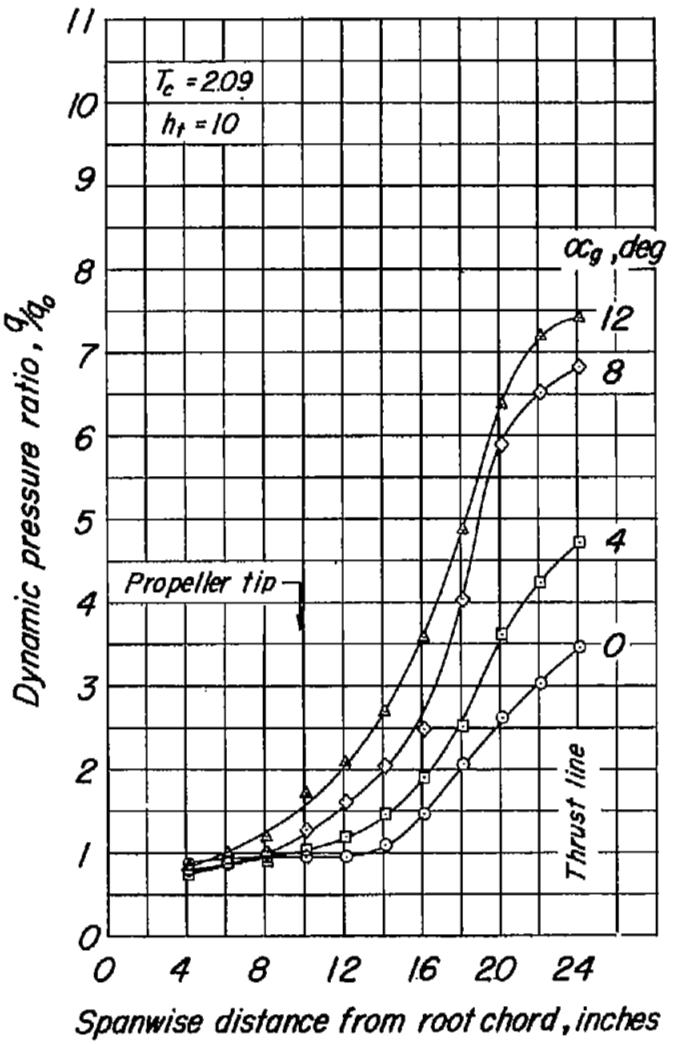

(c) Effect of angle of attack; h_t = 10.

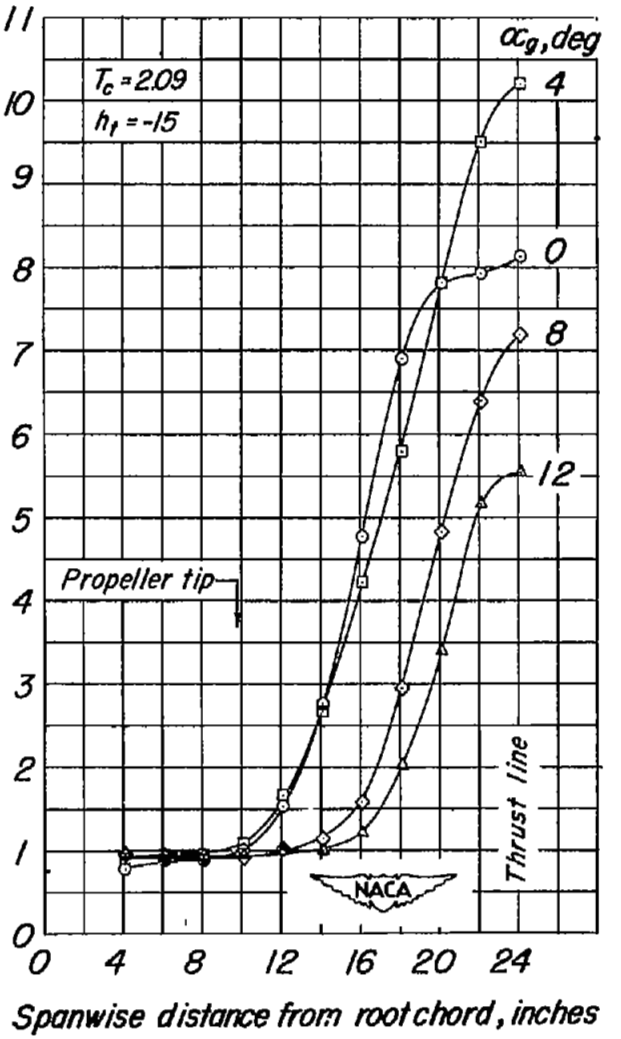

(d) Effect of angle of attack; h_t = -15.

Figure 18.- Concluded.

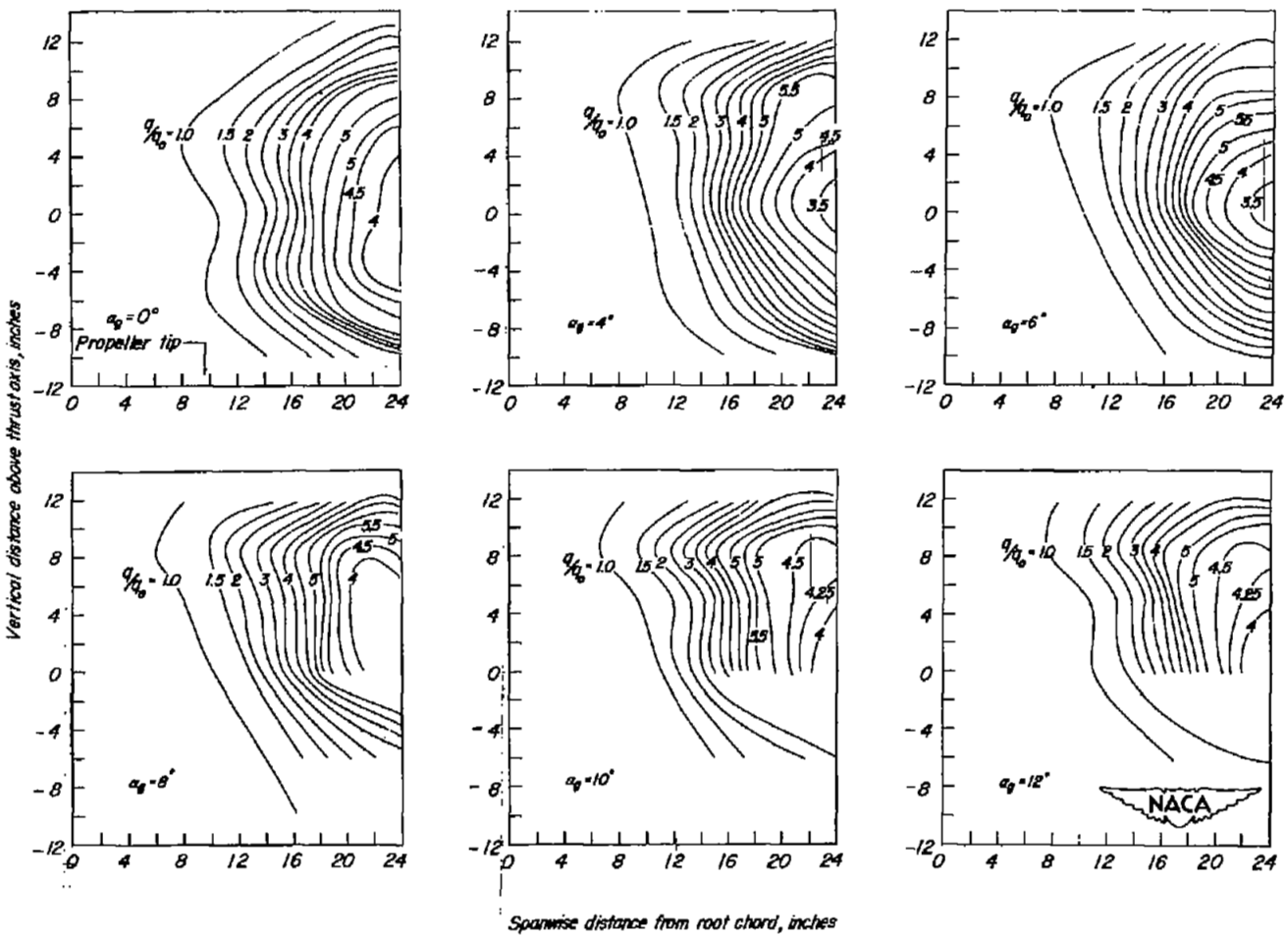

(a) $T_c = 0.90$.

Figure 19.- Contours of dynamic pressure ratio obtained from rake surveys. Inboard-thrust location.

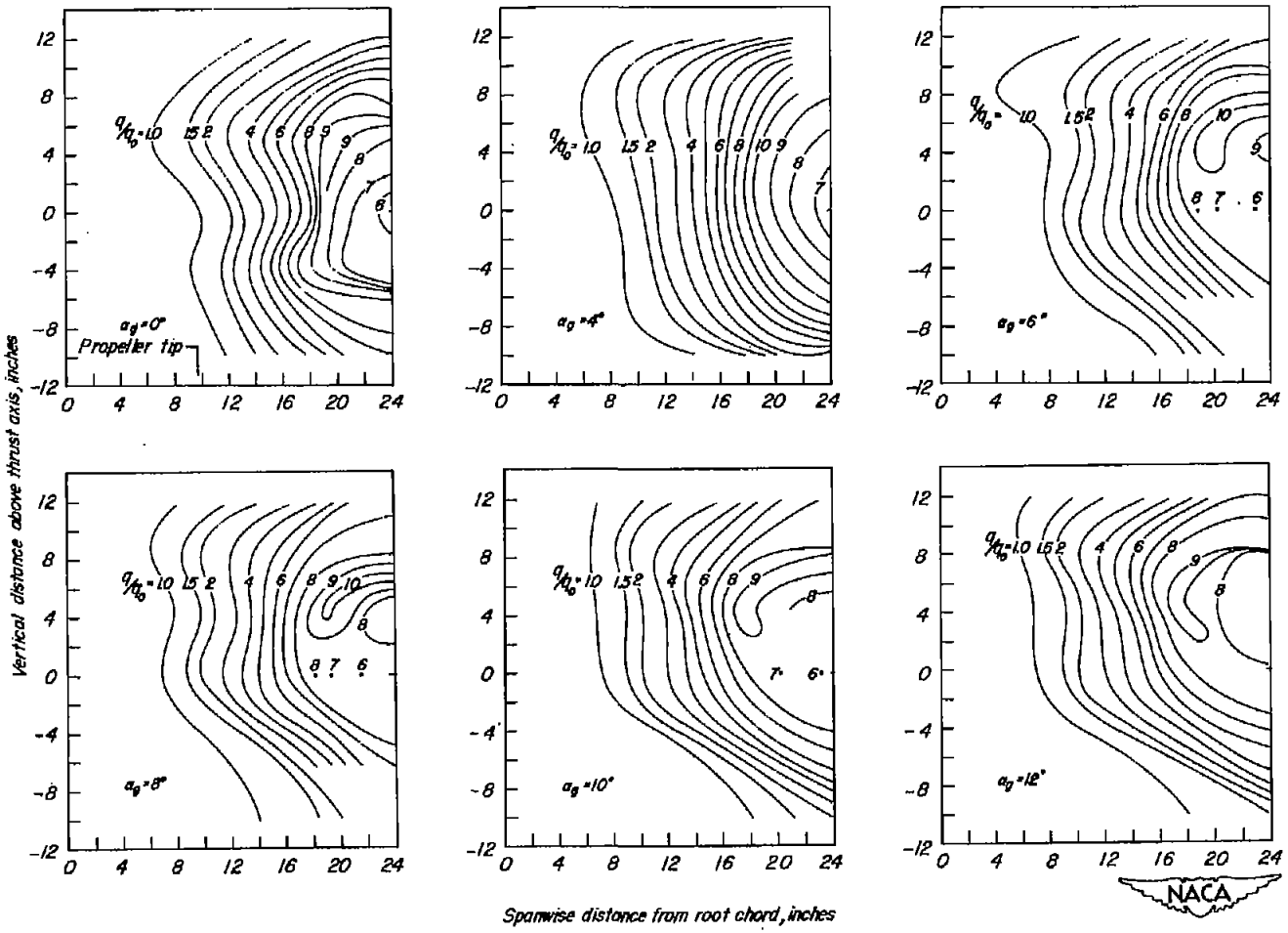

(b) T_c = 2.09.

Figure 19.- Concluded.

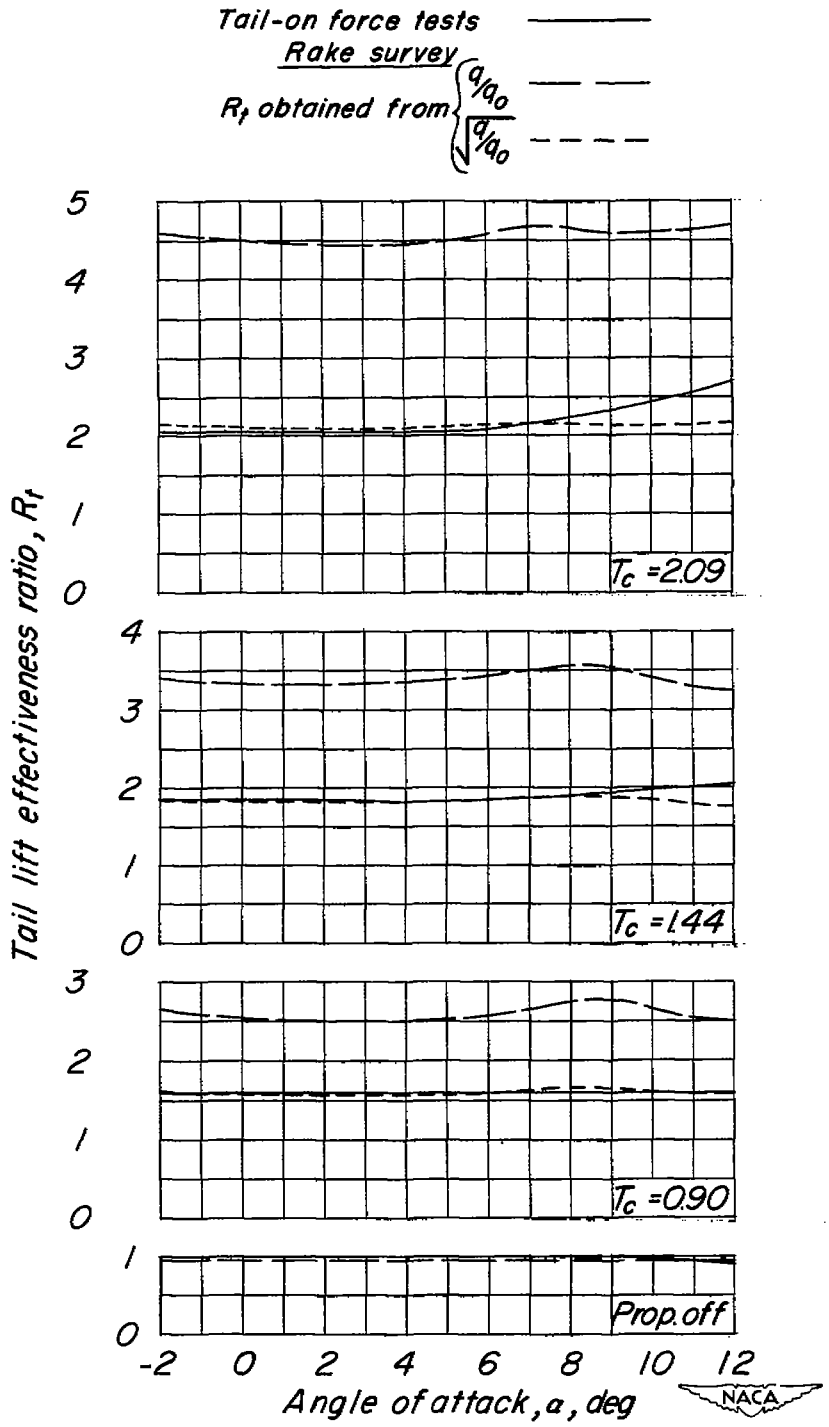

Figure 20.- Comparison of tail lift effectiveness obtained from integrated dynamic pressure surveys and from tail-on force tests. Inboard-thrust location; h_t = 0.

[redacted]

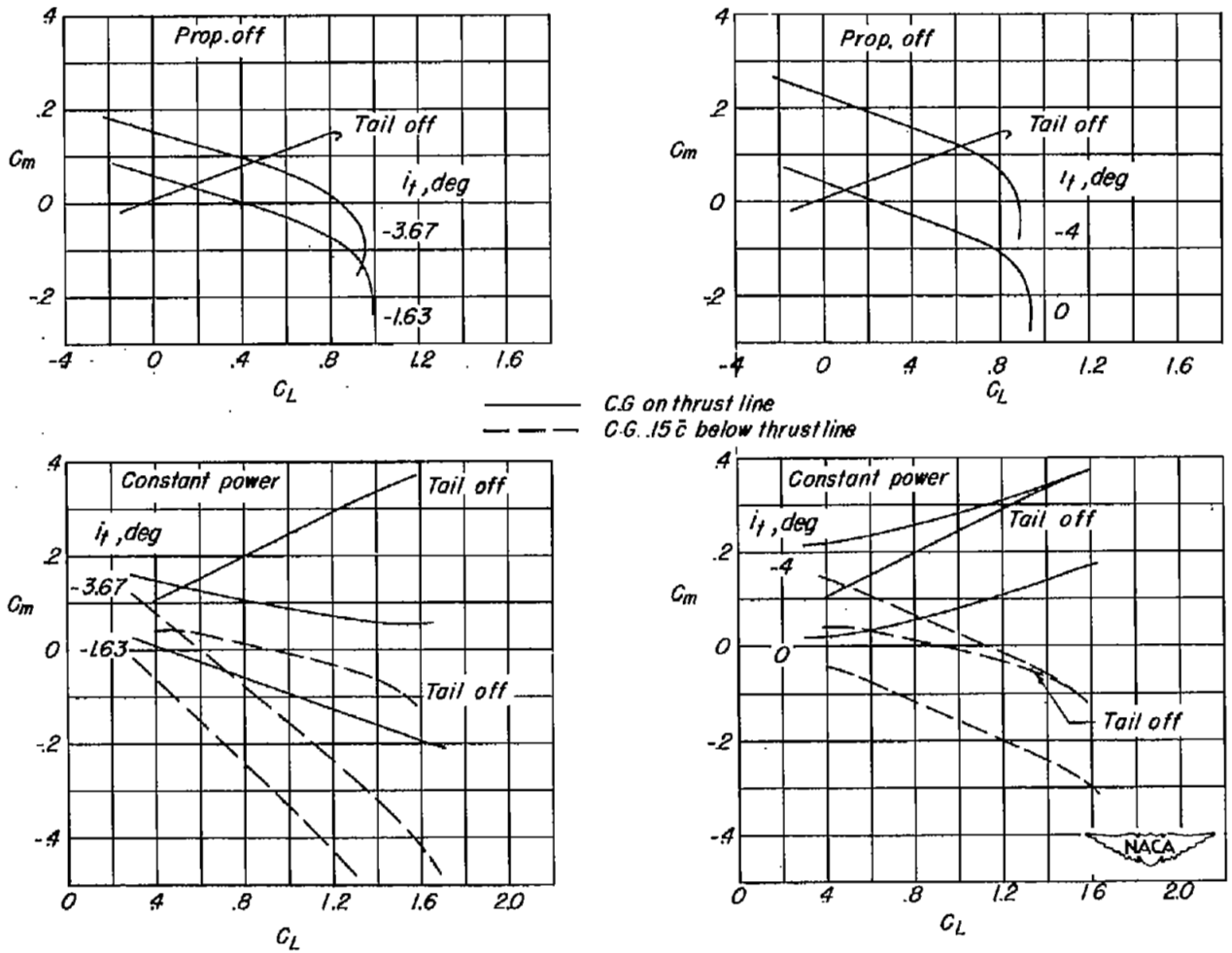

(a) $h_t = 0$.

(b) $h_t = 20$.

Figure 21.- Pitching-moment characteristics for power-off and constant power condition. Longitudinal location of reference center of gravity at 35.8-percent $\bar{c}$; inboard-thrust location.

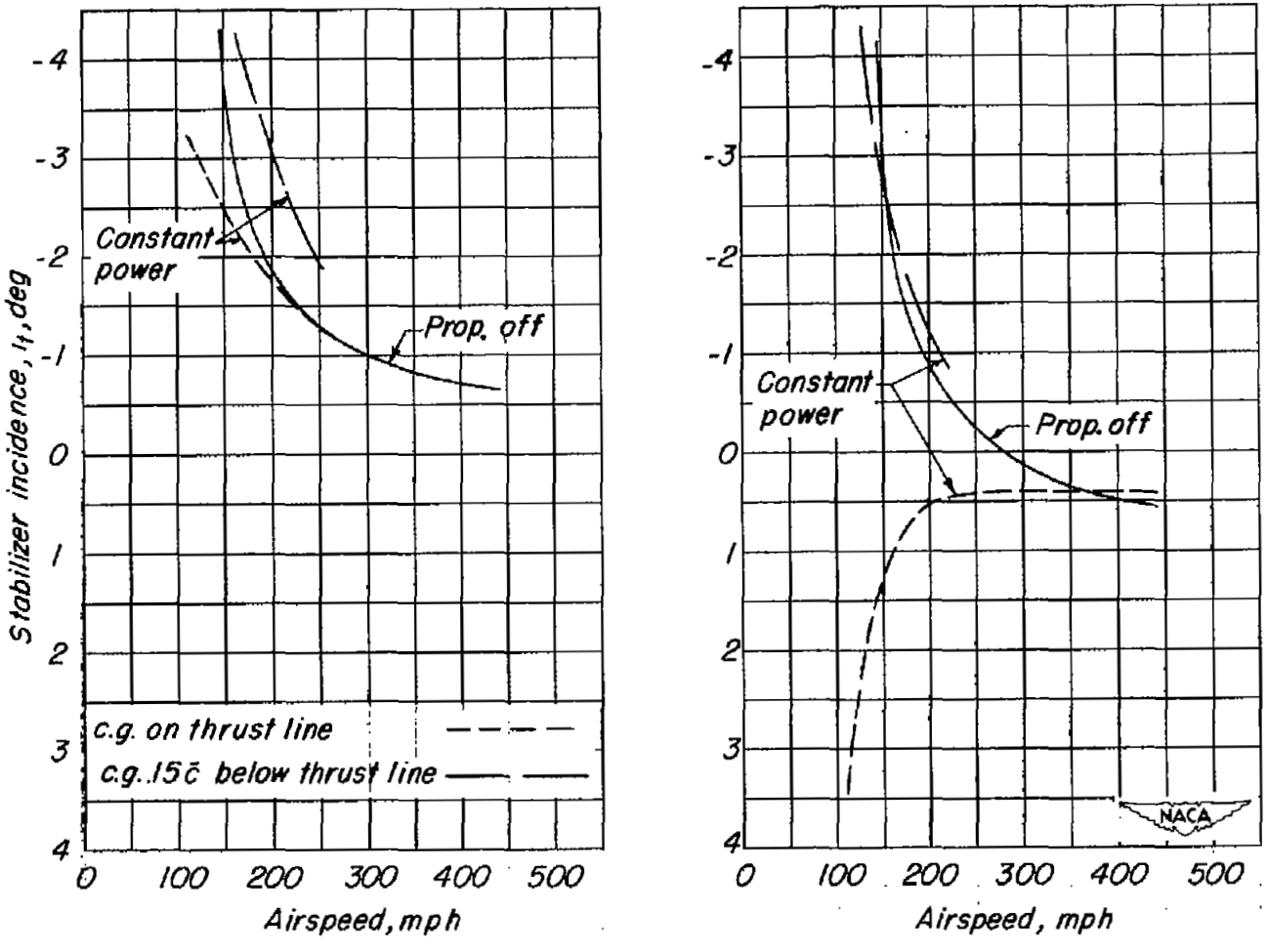

(a) $h_t = 0$.

(b) $h_t = 20$.

Figure 22.- Effects of propeller operation and vertical location of center of gravity on stabilizer setting for trim. Inboard-thrust location; $\frac{W}{S} = 50$.

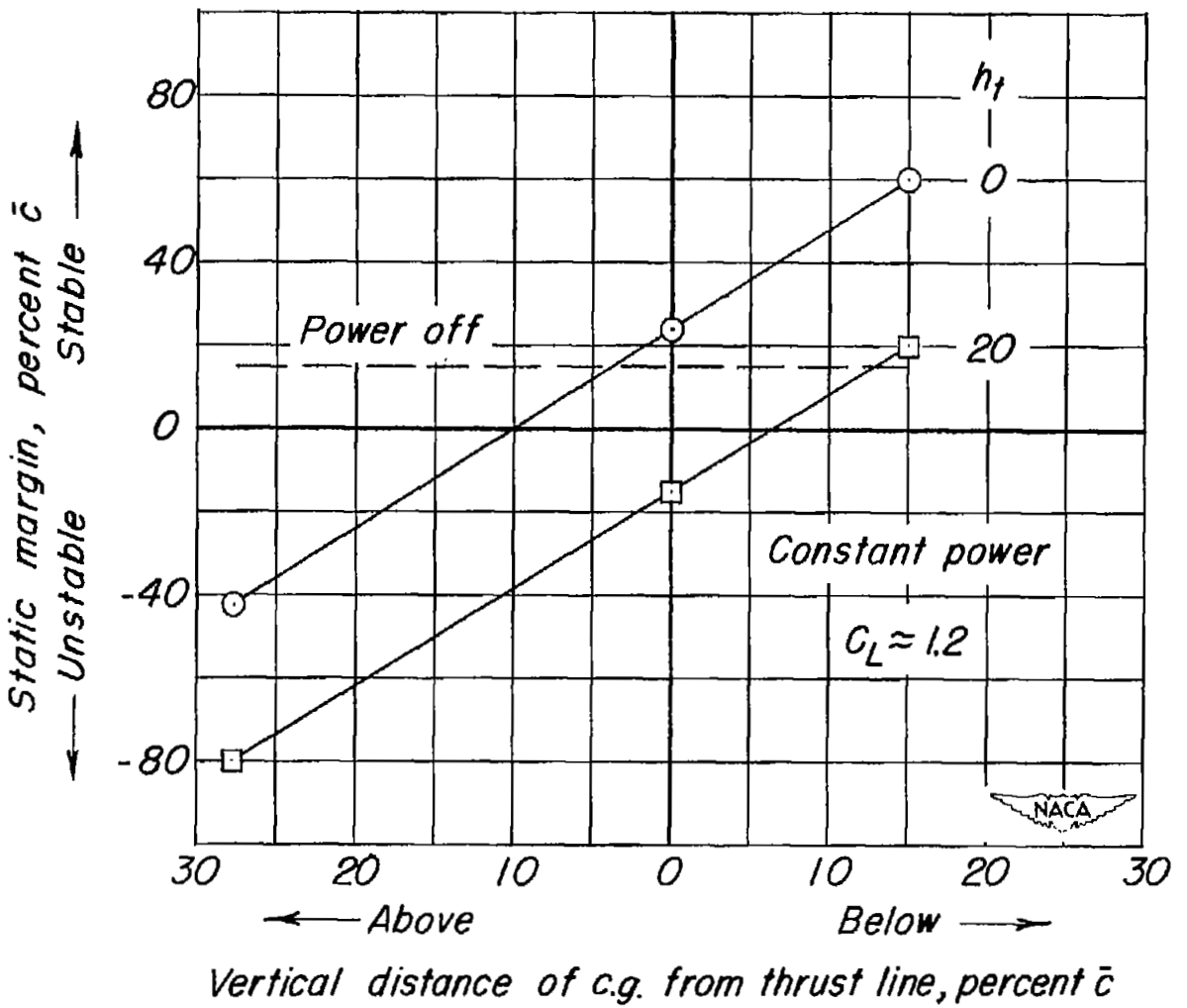

Figure 23.- Effects of center-of-gravity location and tail height on the constant power stability of the semispan powered model. Inboard-thrust location.

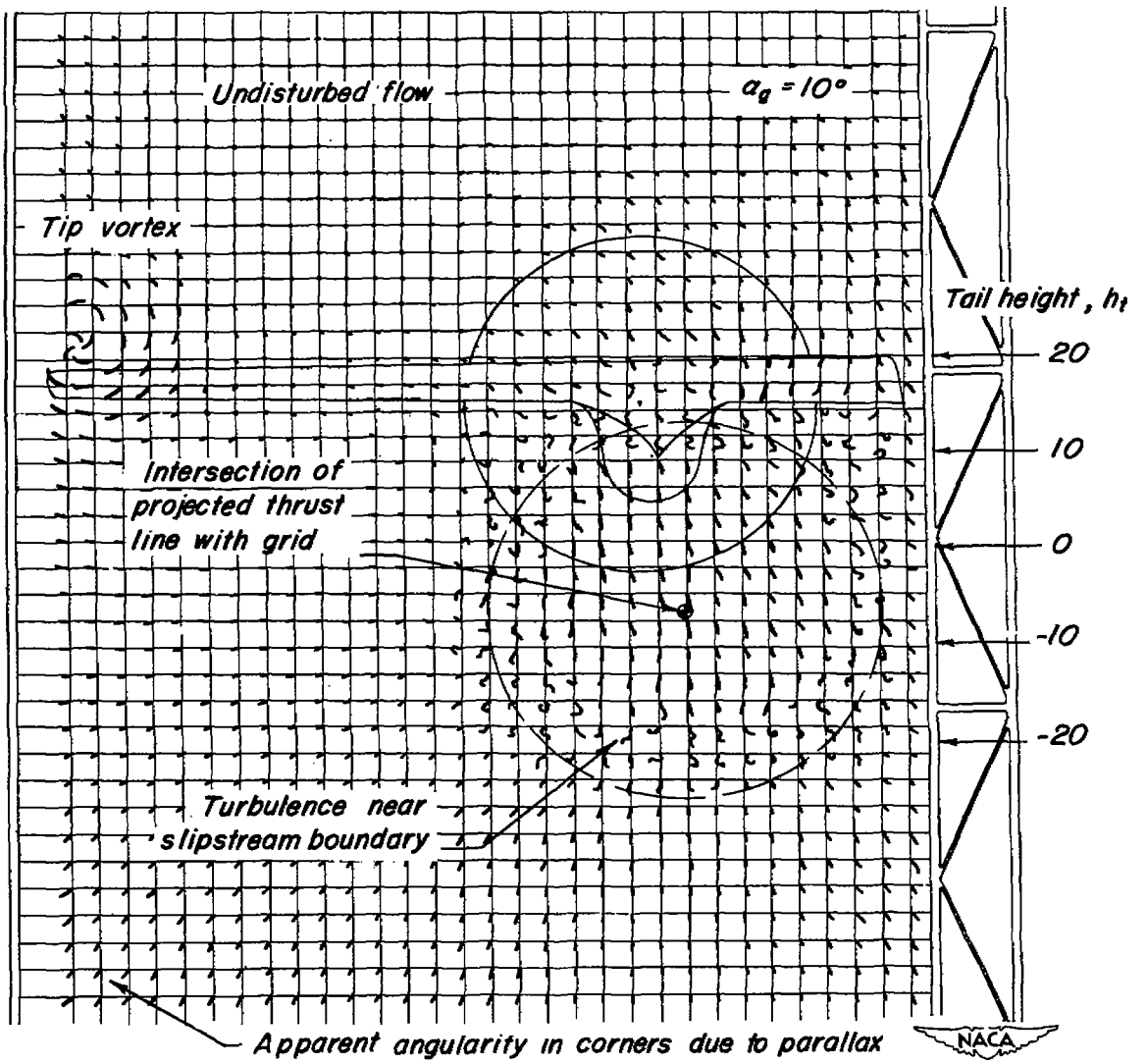

Figure 24.- Sketch of the tuft grid and model showing regions of disturbed flow from the propeller and wing tip. Inboard-thrust location; $\alpha_g = 10°$

[redacted]

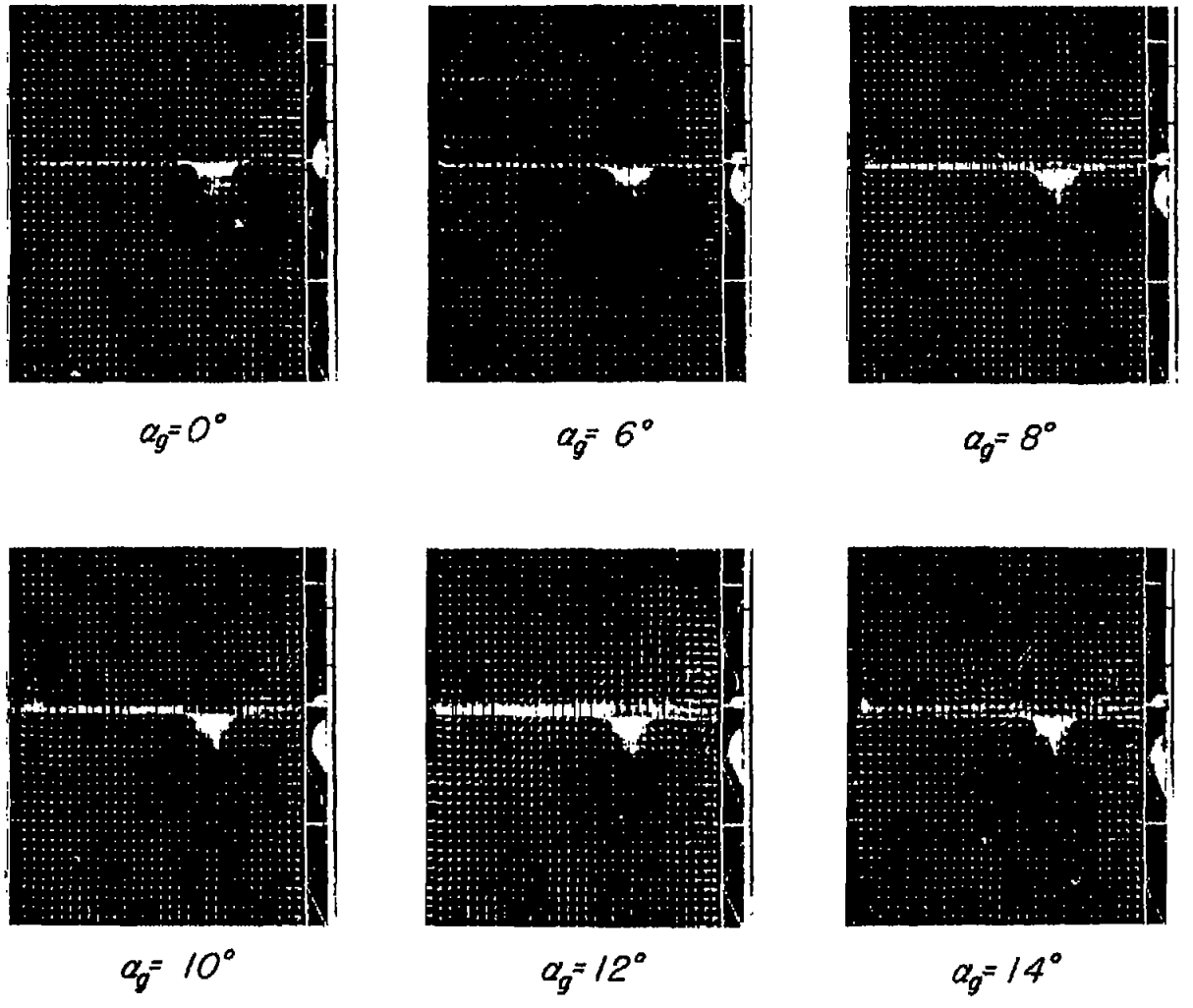

(a) Effect of angle of attack; propeller off.

NACA L-74422

Figure 25.- Tuft grid behind the model with the inboard-thrust location.

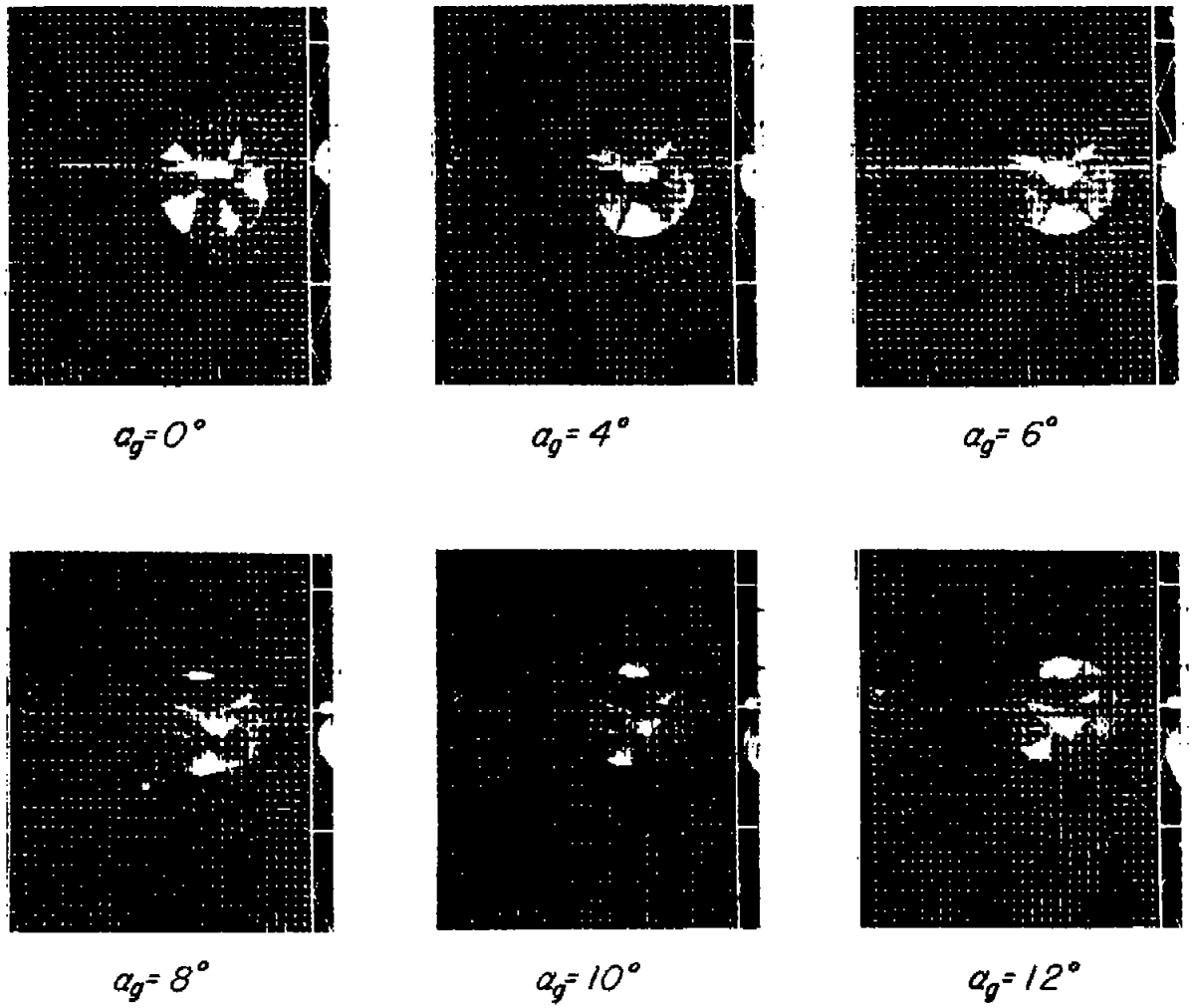

(b) Effect of angle of attack; $T_c = 2.09$.

NACA
L-74423

Figure 25.- Continued.

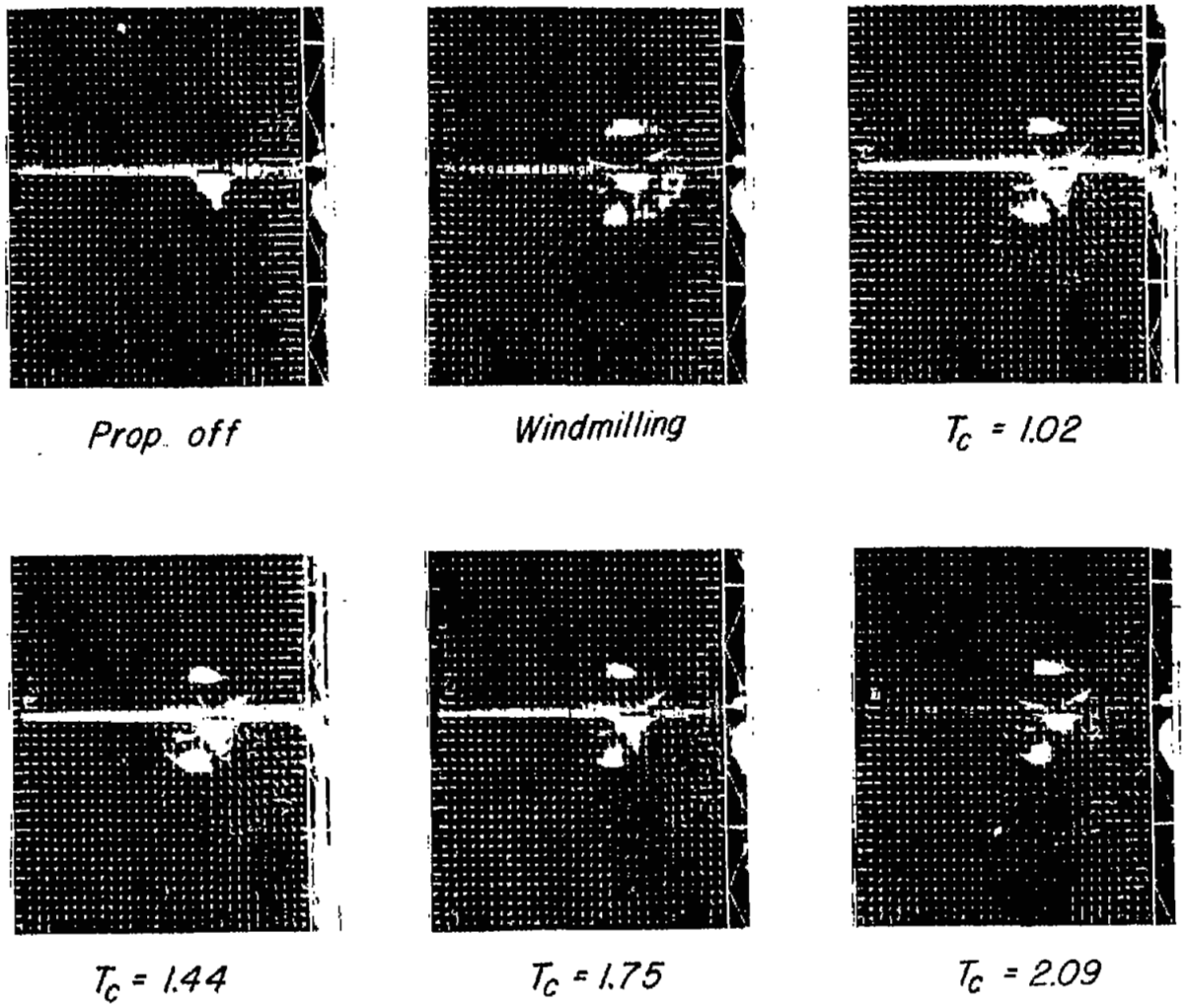

(c) Effect of thrust coefficient; $\alpha_g = 10^\circ$.

NACA L-74424

Figure 25.- Continued.

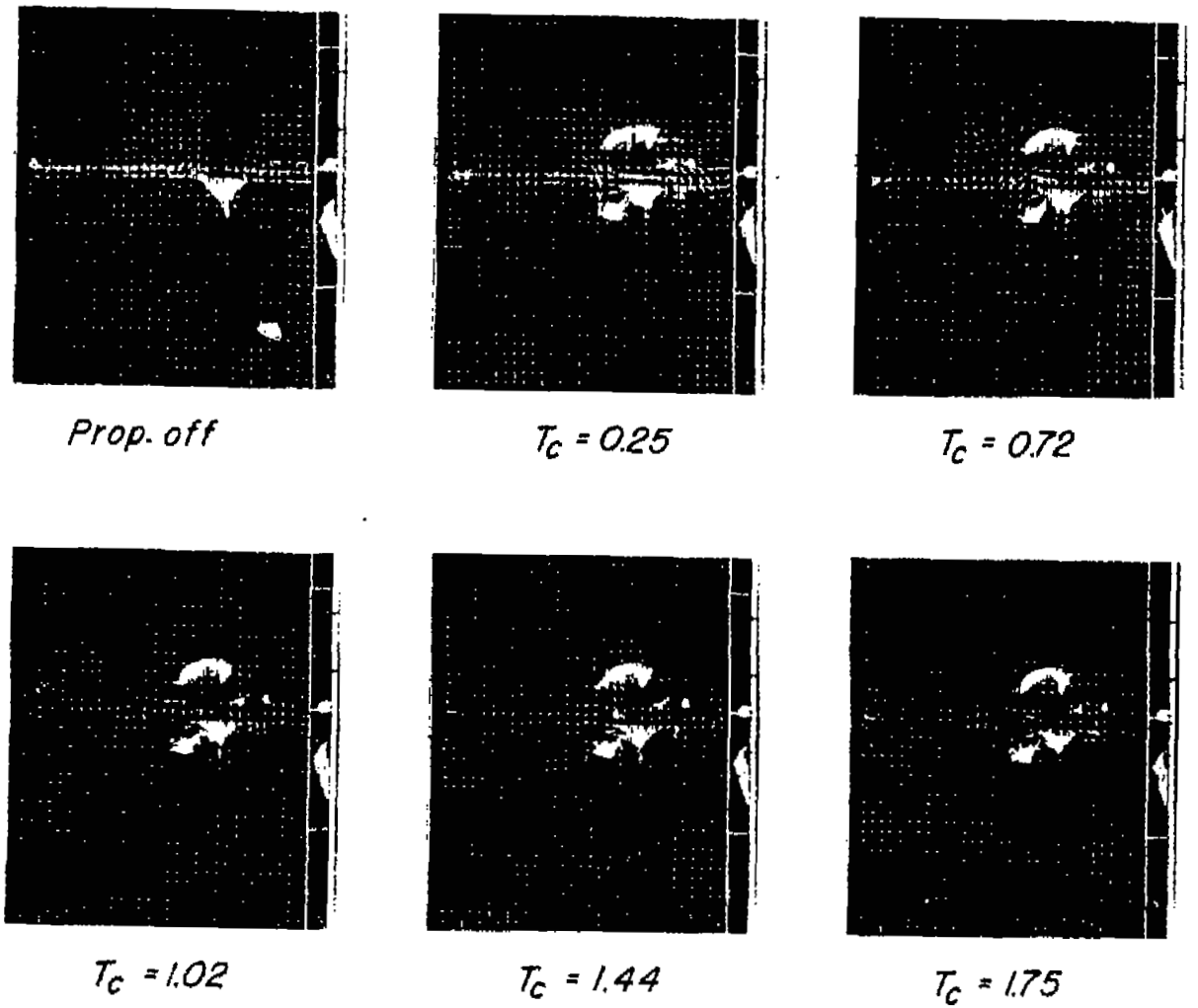

(d) Effect of thrust coefficient; $\alpha_g = 14^\circ$.

NACA
L-74425

Figure 25.- Concluded.

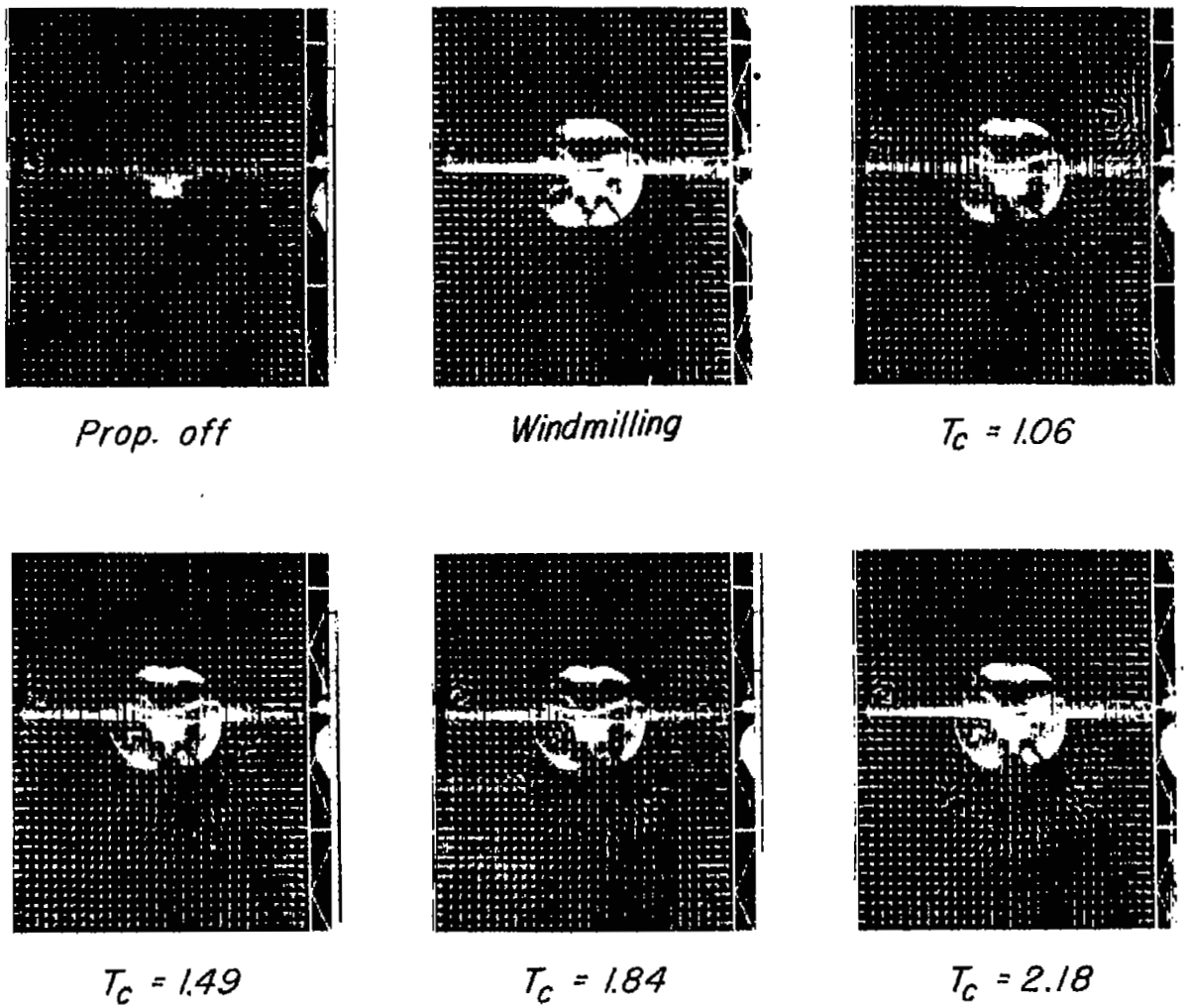

(a) Effect of thrust coefficient; $\alpha_g = 10^o$.

NACA L-74426

Figure 26.- Tuft grid behind the model with the outboard-thrust location.

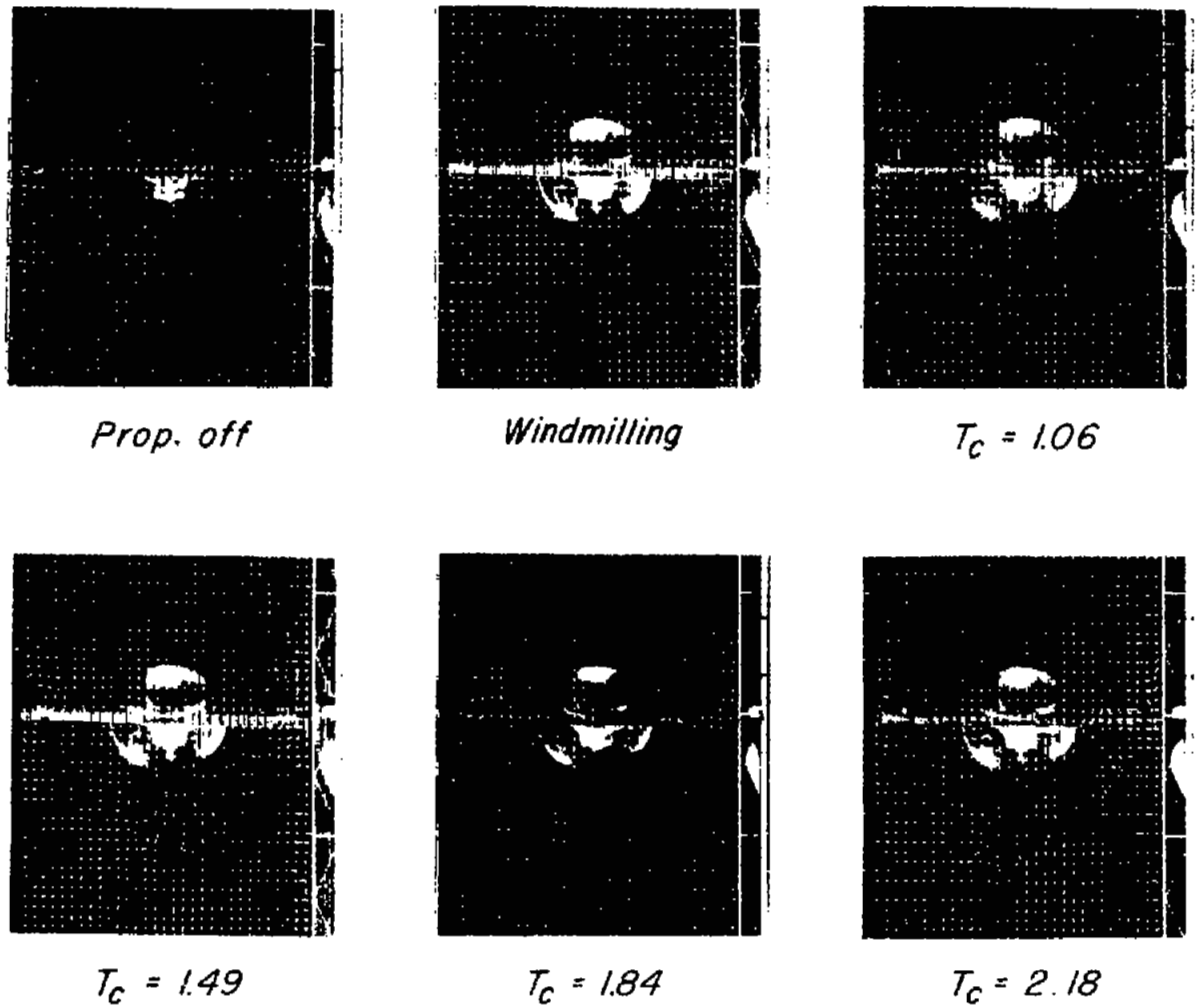

(b) Effect of thrust coefficient; $\alpha_g = 12^\circ$.

NACA
L-74427

Figure 26.- Concluded.

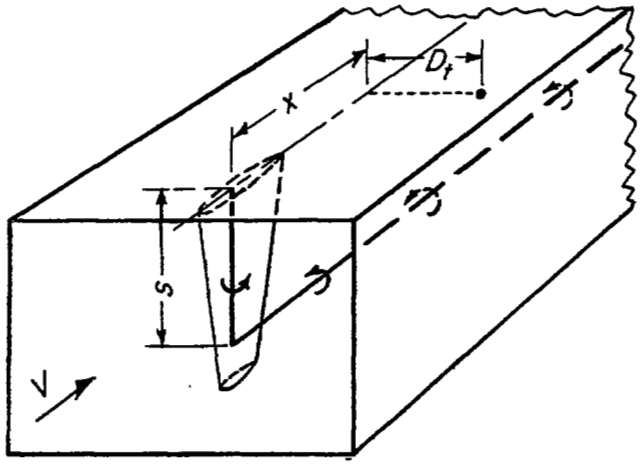

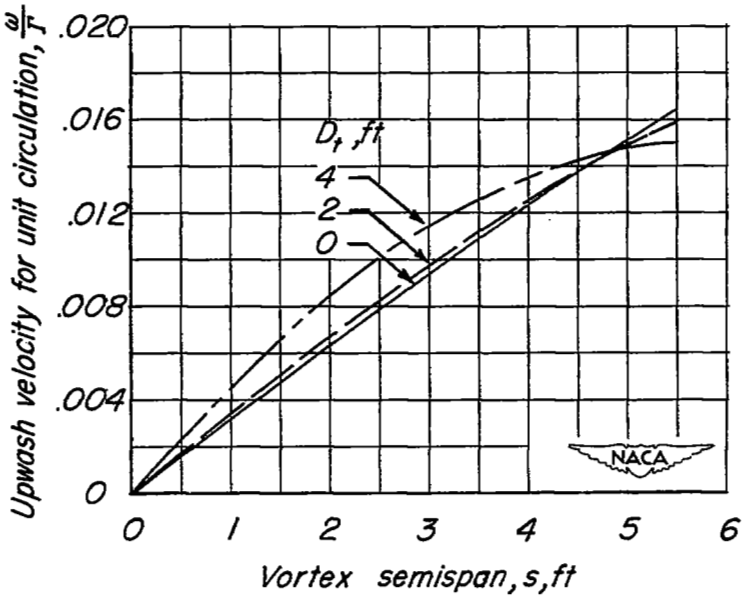

Figure 27.- Sketch defining symbols used and jet-boundary-induced upwash at various distances above lifting line.

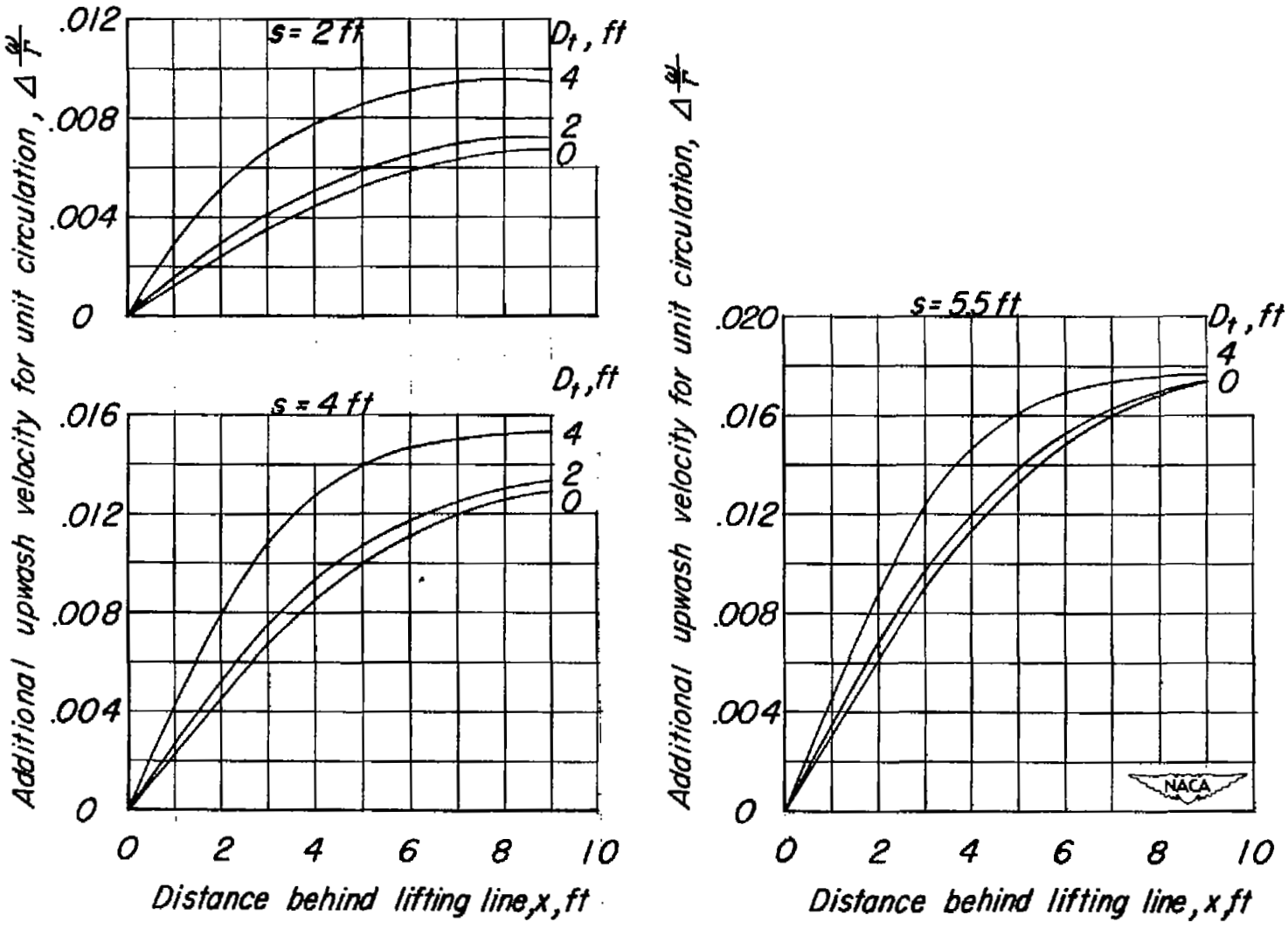

Figure 28.- Additional upwash at various distances behind and above the lifting line.

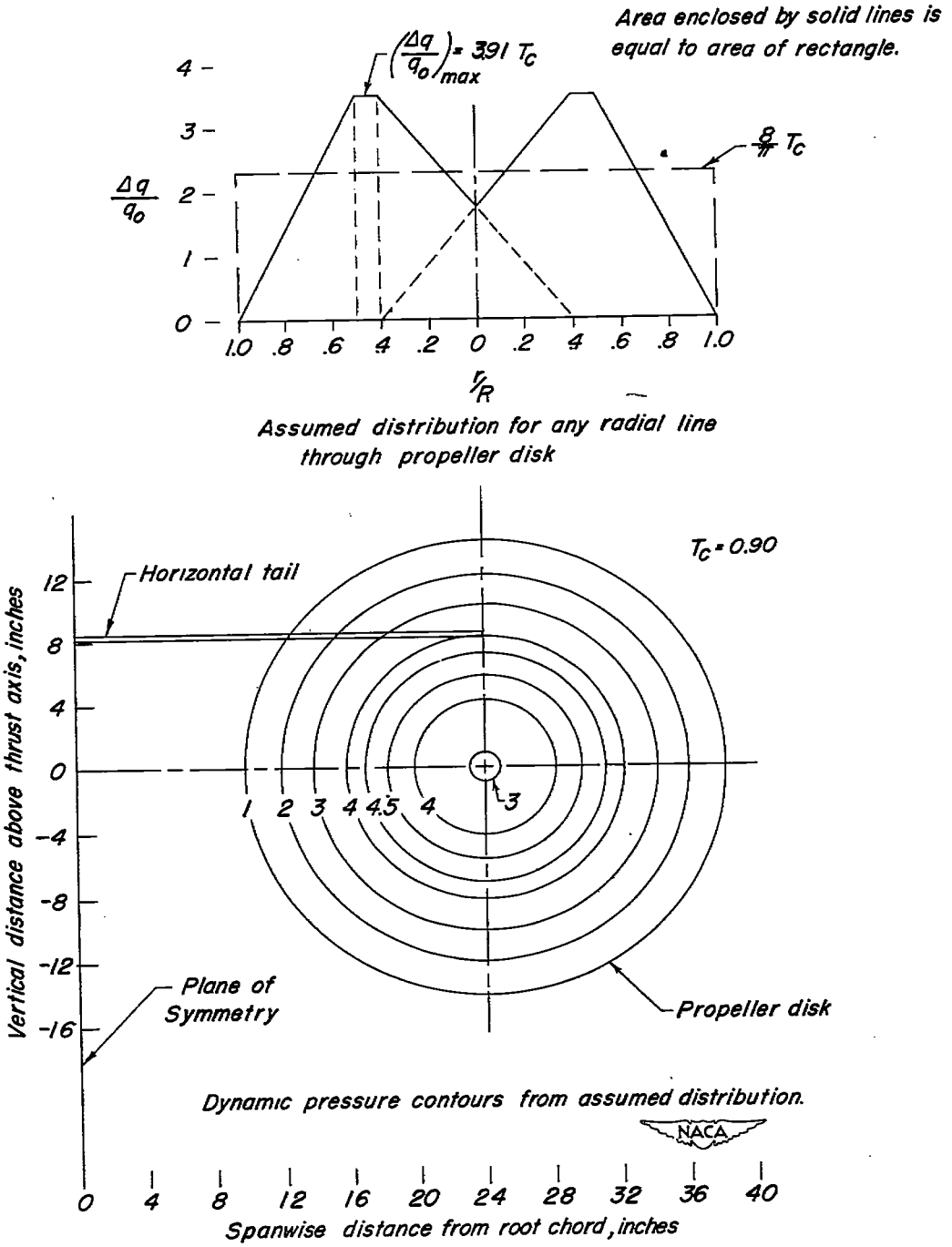

Figure 29.- Estimated dynamic pressure contours for $T_c = 0.90$. Inboard-thrust location; $\alpha = 0^\circ$.

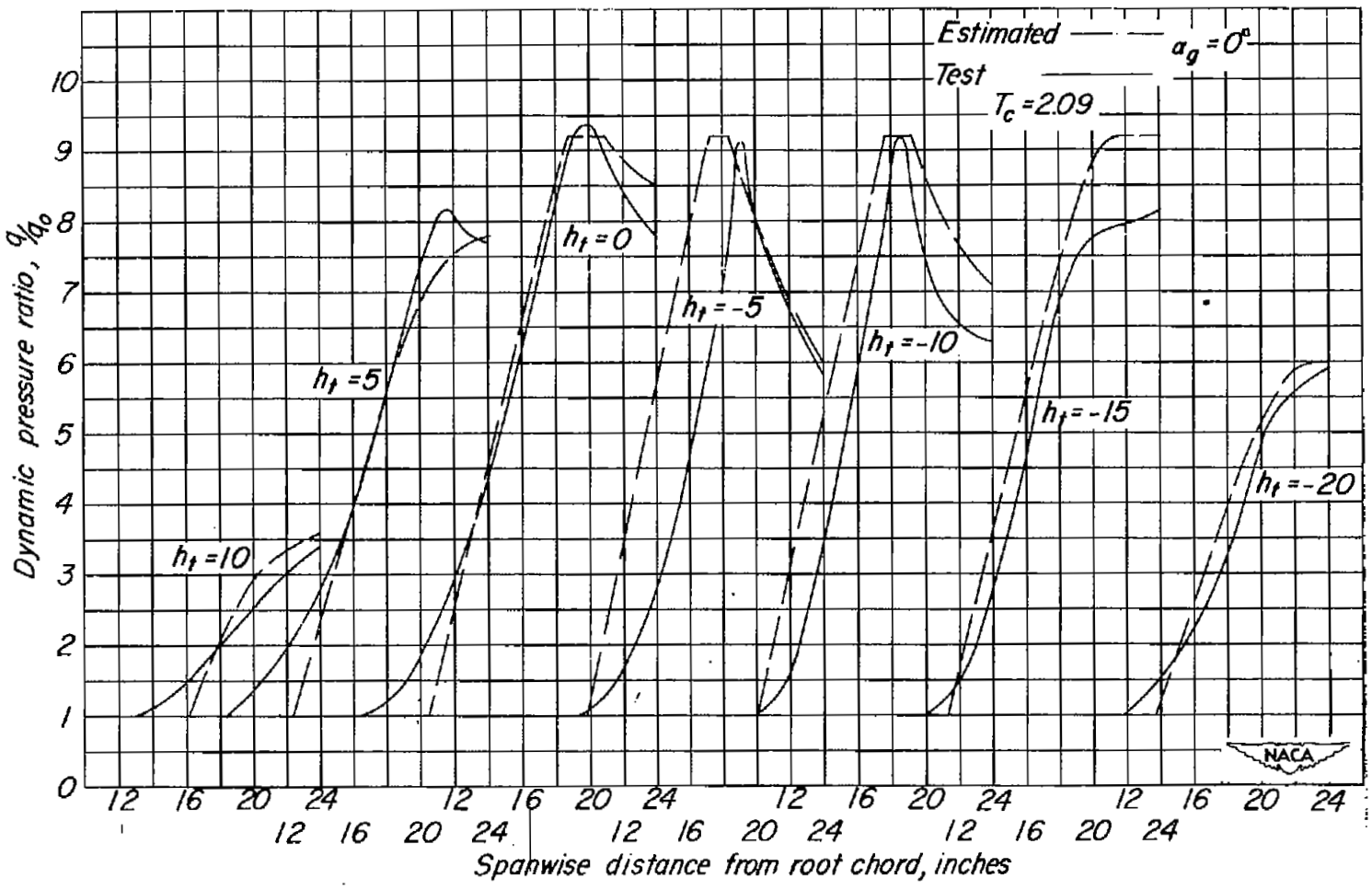

(a) Effect of tail height; $\alpha_g = 0°$.

Figure 30.- Comparison of the estimated and experimental variation of dynamic pressure ratio with tail span. Inboard-thrust location.

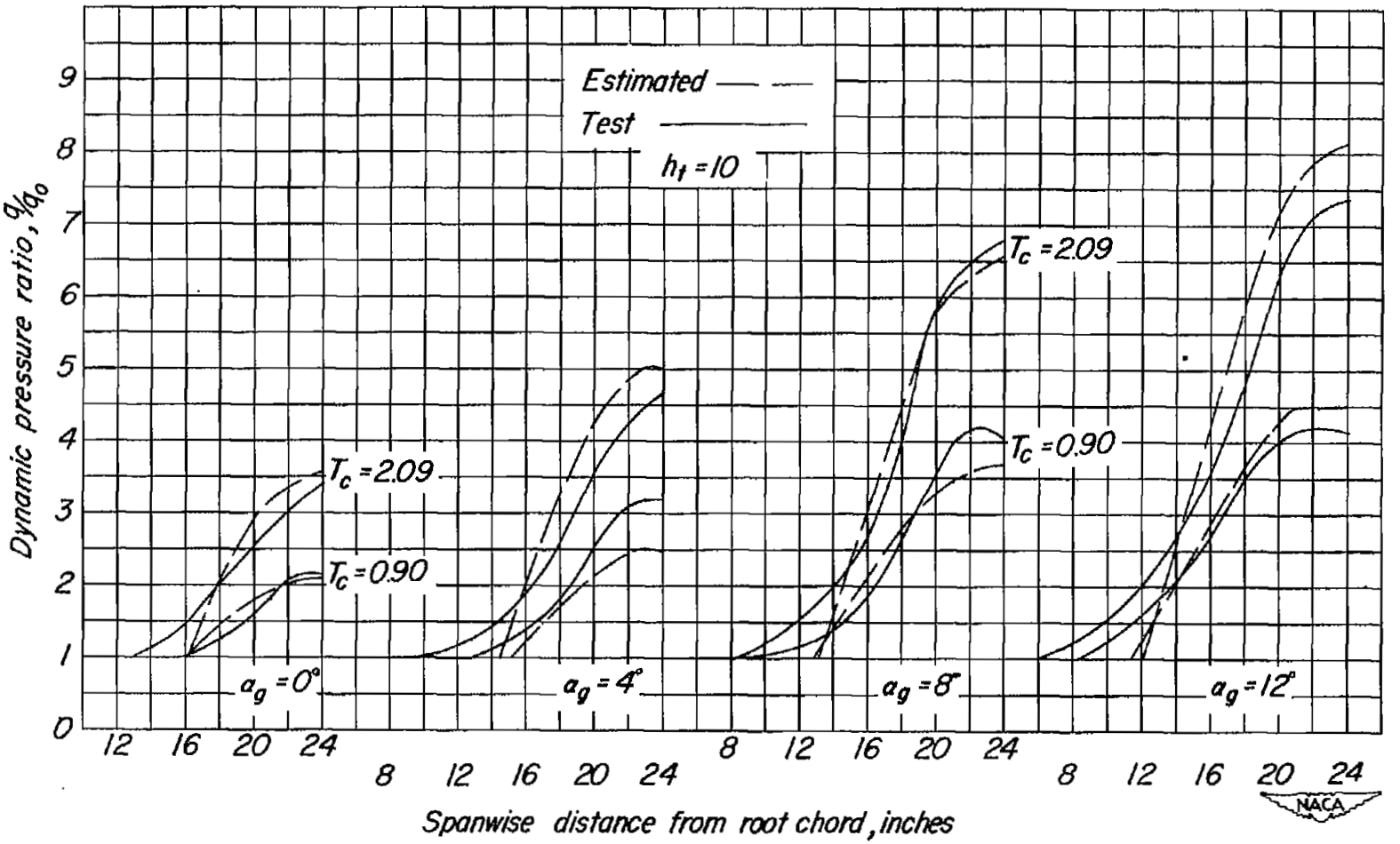

(b) Effect of angle of attack; $h_t = 10$.

Figure 30.- Continued.

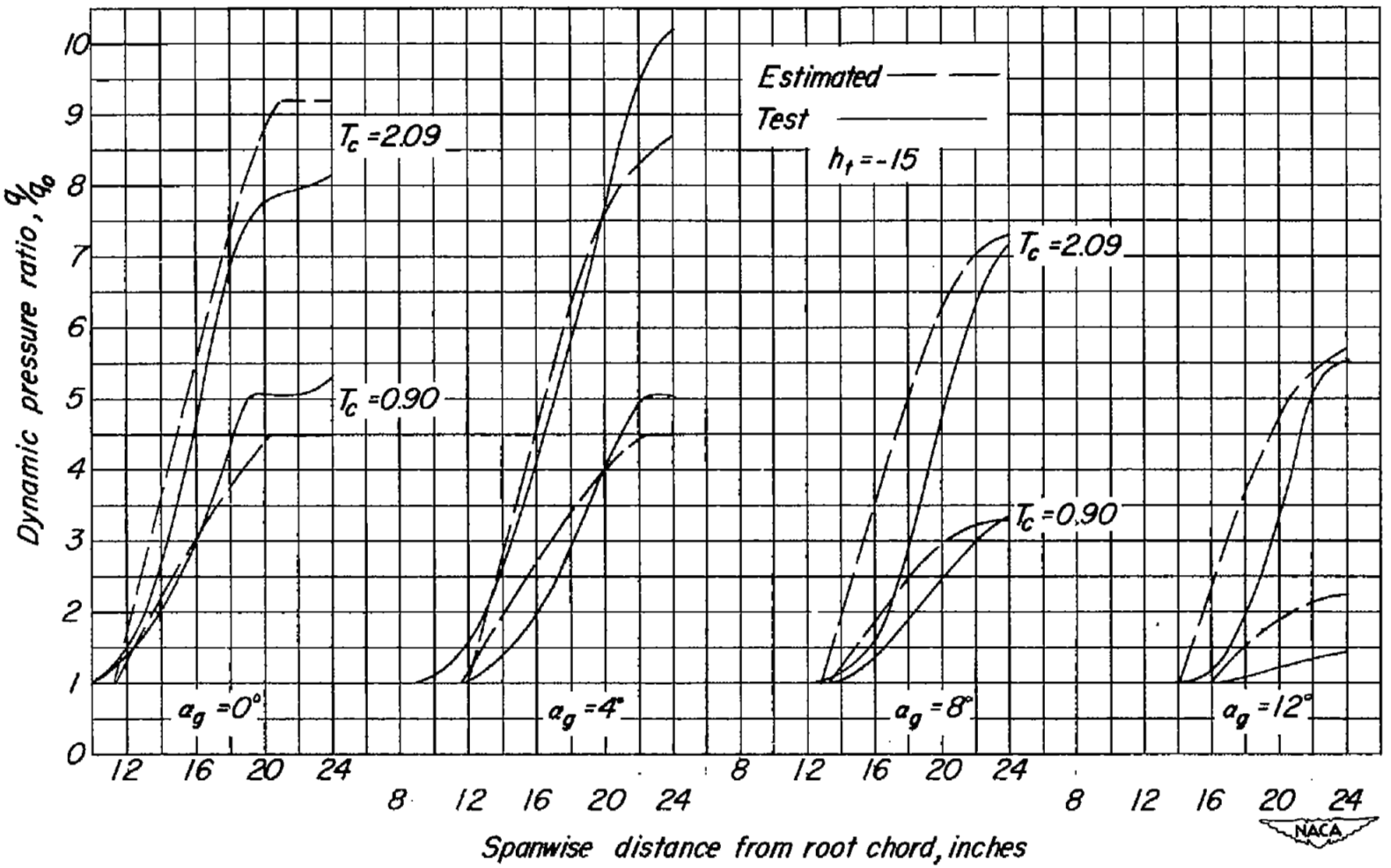

(c) Effect of angle of attack; h_t = -15.

Figure 30.- Concluded.